Charge reconstruction with the AMS-RICH

Elisa Lanciotti
Universidad Complutense de Madrid
Departamento de Física Atómica

june 2003

Contents

Introduction

The Antimatter Magnetic Spectrometer (AMS) is a large acceptance detector designed to operate in space to measure cosmic ray fluxes in low Earth orbit. Primary objectives of the experiment are the search for antimatter nuclei and for the annihilation products of dark matter in cosmic rays with an unprecedented sensitivity.

The first mission of the experiment consisted in a precursor flight of 10 days in june 1998 [3] aboard the space shuttle Discovery, to test the feasibility of the experiment. An upgraded version of the detector will be launched for a second long duration flight aboard the International Space Station (ISS) scheduled for the end of 2005.

For this mission AMS will be equipped with a Ring Imaging CHerenkov (RICH) detector. The goal of the RICH is to perform particle velocity measurement with a resolution of about 0.1% for unit charge particles and charge measurement up to Iron.

The aim of this report is to study the RICH capabilities for charge reconstruction in a wide range of charge.

The structure of this work is the following: in chapter 1 an introductory overview on the physics of cosmic rays is given, and different detection technics are discussed. In chapter 2 the motivation of this experiment is introduced and the experiment AMS and its subsystems are briefly described. Chapter 3 is devoted to the RICH detectors, with special emphasis on the RICH of AMS-02.

In chapter 4 the assumptions at the basis of the method of charge reconstruction are explained and the structure of the algorithm implemented in the RICH simulation software is discussed. Then, some results obtained on the simulation of the RICH flight setup are shown.

In chapter 5 some preliminary results with data of the RICH prototype will be illustrated to confirm the detector capabilities and the validity of the reconstruction algorithm.

Finally, the conclusions of this work are presented.

Chapter 1

Cosmic rays and their detection

1.1 Introduction on cosmic rays

Cosmic rays (CR) are high energy particles of extra-terrestrial origin. The flux of CR at the top of the atmosphere is composed mainly of ionized nuclei (98%) and a small fraction of electrons (2%). The nuclear component consists of a 87% of protons, the most frequent particle in CR, a 12% of helium and a 1% of heavier ions [50]. In this section an introductory overview on CR will be given[1], starting from the description of their energy spectrum. Then, considering the differences among the spectra of individual species, the distinction between primary and secondary CR will be introduced and their different origin and propagation will be discussed.

Finally, the extremes of the energy spectrum are considered, on both sides of very low and very high energy.

1.1.1 The CR spectrum

At a first glance, the most outstanding feature of the CR spectrum (see figure 1.1 left panel) is its very regular shape which, to a good approximation, follows a power low in energy:

$$N(E)dE = KE^{-\gamma}dE \tag{1.1}$$

where E is the energy per nucleon, K is a constant, and γ the spectral index. The value of γ is 2.7 up to $E \sim 10^7$GeV, where the slope has a

[1] See [27] for a comprehensive discussion about cosmic rays.

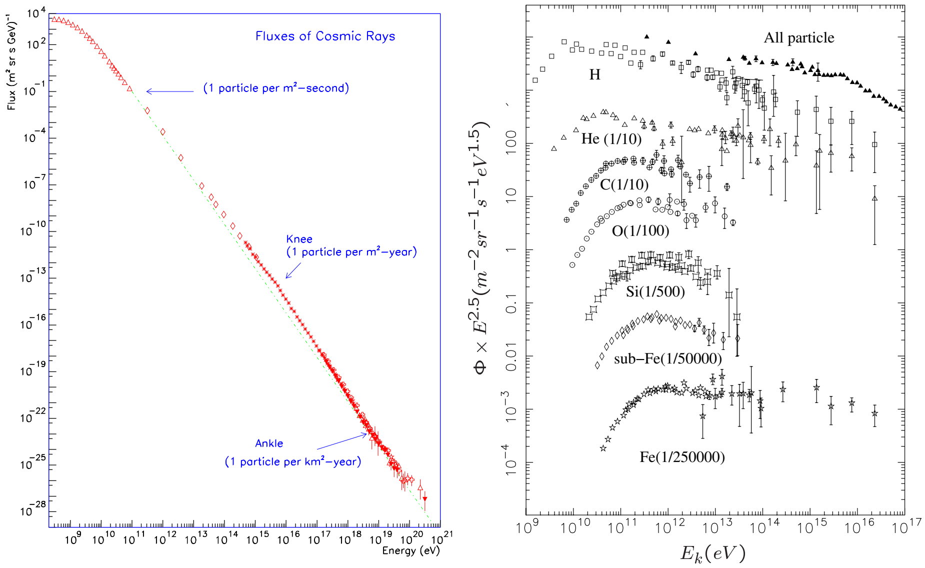

Figure 1.1: CR spectrum: on the left the total flux of the CR, on the right the flux for different species multiplied by $E^{2.5}$ to flatten the spectrum.

sudden change (the "knee" of the spectrum). For energies above the knee the spectrum becomes steeper and γ is measured to be 3, up to $E \simeq 10^{19}$ eV. At this point, called the "ankle", the slope changes back to 2.7. All the particle species have approximately the same behavior, in accordance with a common origin for all them.

1.1.2 Primary and secondary CR

From figure 1.1, right panel, it can be noticed that the energy spectrum for all the elements present in cosmic rays follows a power low. However there are remarkable differences in the shape of the spectrum and in the abundance of the different elements. Usually the spectrum of Iron is taken as reference, due to its high abundance. Some other species show a very similar behavior, like Nickel or Carbon, whereas other species like Vanadium, Scandium, Boron, have a steeper spectrum. This fact reveals the fundamental difference between primary and secondary cosmic rays. Primary cosmic rays, like Iron, are particles produced and accelerated at the very initial sources of cosmic rays, most probably Super Nova Remnants (SNR) (see later in

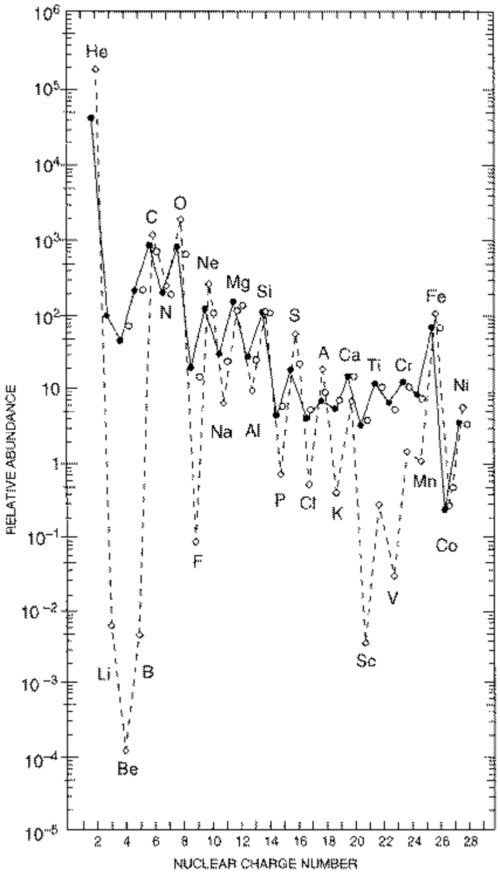

Figure 1.2: Abundance of cosmic rays measured near the Earth (continuous line) and in the solar system (dashed line). All the points are normalised to Si=100.

section 1.1.3), whereas secondary CR are absent in stellar environment and are produced by fragmentation of heavier nuclei during their propagation.

Comparing the relative quantity of different elements at the source and near the Earth, and considering the cross sections for spallation and all the interactions with the interstellar medium (ISM) one can obtain an estimate of the quantity of matter traversed by cosmic rays from their origin to the detection site. The mean quantity of matter traversed amounts to about X=7g/cm^2. The density of the disk of the Galaxy is estimated as ρ=1 proton per cm^3, thus the distance a particle travels before interacting, with the hypothesis of a rectilinear trajectory, would be:

$$l = \frac{X}{m_p \rho} \sim 10^3 kpc$$

This distance is much larger than the radius of the galaxy (about 30 kpc) so it can be inferred that CR are deflected by the galactic magnetic fields following bended trajectories and are confined for a very long time inside the Galaxy before escaping outside or interacting [43]. The repeated magnetic deflection also explains why we see an isotrope flux of cosmic rays.

1.1.3 Origin and propagation

The origin of CR is still an open issue. Many energetic sources, such as Super Novae (SN) explosions, quasars, radio galaxies, pulsars, Gamma Ray Bursts (GRB) have been proposed as candidates of CR sources.

It is commonly believed that most of the CR are generated in SN explosions [5]. The acceleration of ionized nuclei takes place in spherical shocks caused by the explosion, where the charged particles are cycling back and forth across the shock region. During this process, known as "first order Fermi acceleration", the particles gain kinetic energy with high efficiency. This mechanism naturally provides a power law for the energy spectrum of the accelerated particles, just as observed in experimental data. The energy generated by a SN explosion (10^{44} J) can account for the power needed to keep steady the CR ray flux, considering that the rate of such explosions is one every 30 years. These arguments make the hypothesis of SN very appealing.

The change of slope at energy about 10^{15}eV is due to a loss of efficiency of the Fermi mechanism in accelerating particles above such rigidity. Also the rigidity dependent confinement mechanism contributes to the steepening of the spectrum: the probability for a charged particle to escape from the galactic magnetic field ($\simeq 3\mu g$) increases with the particle rigidity ($p_{esc} \propto E^{0.7}$). For the same reason it is probable that part of the CR beyond the knee region are of extra galactic origin. There is not yet a common consensus on this topic, due to the lack of good experimental data in that energy region.

Once injected in the Galaxy, CR travel through tortuous paths before escaping. During the confinement time CR particles interact with the components of the ISM, such as gas, magnetic fields and photons. Nuclear interactions with protons of the ISM (process known as "spallation") produce secondary CR (as anticipated in section 1.1.2). Heavy nuclei break originating lighter nuclei: Boron, Beryllium and Lithium arise from Carbon and Oxigen, whereas Scandium, Vanadium, Titanium, Manganese are produced by Iron interactions. If we compare the relative abundance of the elements in CR and in the solar system[2] (see figure 1.2) we see that the elements believed to be secondary (like Li, Be, B) are almost absent in the solar system. The B/C ratio is the observable quantity representative of the secondary to primary ratio. The study of its evolution with the energy is source of important information for all CR propagation models.

Another important issue of seconday CR is that some species created in the spallation reactions are radioactive and their abundances can be used to estimate the "age" of the sample of CR near the Earth and, in turn, the confinement time in the Galaxy. The most appropriate isotope for this task is the ^{10}Be which decays in ^{10}B with a mean lifetime $\tau_r = 2.2 \times 10^6$ years, comparable with the confinement time. Therefore, from the relative abundance of Be isotopes one can infer the quantity of ^{10}Be that has decayed and estimate the age of that sample, which results to be $\sim 10^7$ years. For this purpose it would be suitable to have more precise measurements of the different isotopes of Beryllium (up to date the isotope ^{10}Be has been separated only up to energy 1.5 GeV/n with 20–30 % accuracy).

1.1.4 The extremes of the energy spectrum

One striking feature of the CR spectrum is the very wide energy range. The arguments discussed so far are valid for CR of intermediate energies; in this section some aspects of the very low and very high energy spectrum respectively will be outlined.

Very low energy

At energy lower than 1 GeV the spectra of all particle species suffer a strong attenuation. The point where the cutoff is located and its intensity depend on the phase of the solar cycle: flux attenuation is maximum in the phase of maximum solar activity. This phenomenon is due to the influence of the solar

[2]the chemical abundances in the solar system are derived from the photosphere of the Sun, by observing the absorption lines superimposed to the underlying Planck spectrum.

wind on the propagation of CR through the heliosphere[3]. The interactions of CR with the particles forming the solar wind are at the origin of solar modulation. The most relevant phenomenon related to the solar modulation is the behavior of the "anomalous cosmic rays". This effect consists in an excess of the He flux at energy below 60 MeV only observable in periods of low solar activity. A model for the anomalous cosmic rays was proposed by Fisk [20] who suggested that anomalous CR are non fully ionized nuclei carried by the solar wind to the outer heliosphere where they are accelerated by the heliospheric termination shock [25]. The result of this process is that these singly charged atoms have been accelerated and have a magnetic rigidity higher by a factor Z with respect to an atom with the same atomic number but fully ionized, so they arrive closer to the Earth than galactic CR of the same energy, and give rise to a total flux higher than expected.

Anomalous CR only are visible in periods of minimum solar activity, since their production and acceleration depend critically on the solar wind dynamics.

Very high energy

The ultra high energy part of the spectrum extends up to energy $E \sim 10^{20}$eV. This break is known as Greisen-Zatsepin-Kuzmin (GZK) cutoff and is due to the energy loss of protons for interaction with low energy photons of the cosmic microwave background radiation (CMB):

$$p + \gamma \rightarrow \Delta \rightarrow p + \pi^0 \, or \, n + \pi^+ \tag{1.2}$$

the resonance Δ decays either in neutral pions and a proton or in a neutron and a positive charged pion. The energy threshold for this reaction is 5×10^{19}. The mean free path for a single scattering can be computed as $\lambda = 1/\sigma_{\pi p} N_{photon} \simeq 3$ Mpc, where $\sigma_{\pi p}$ is the cross section for this reaction, and N_{photon} the density of photons of the CMB. Considering that in each reaction the fractional energy loss of the proton is $\Delta E/E \simeq 1/10$ one can infer that the most energetic cosmic rays cannot come from sources further than 30 Mpc, which corresponds to the local supercluster of Virgo.

The origin of ultra high energy cosmic rays (in the energy region from the ankle up to the GZK cutoff) is still not clear. One hypothesis is that they

[3]the spherical zone with center in the Sun and radius 100 AU. 1 AU= 1 astronomical unit$\sim 150 \times 10^6$ km

are of extra galactic origin [35]: protons are accelerated in the core of active galactic nuclei, then make a transition to neutron in a photon-proton collision and can escape outside the parent galaxy as a neutral particle. Then, once outside their galaxy, they decay back to protons. This mechanism explains the great majority of protons in CR flux at ultra high energies. Another possible hypothesis postulates that these very energetic particles could be reaccelerated in a galactic wind shock during their propagation [24]. Finally, other authors [36] make the hypothesis of acceleration by powerful radio galaxies.

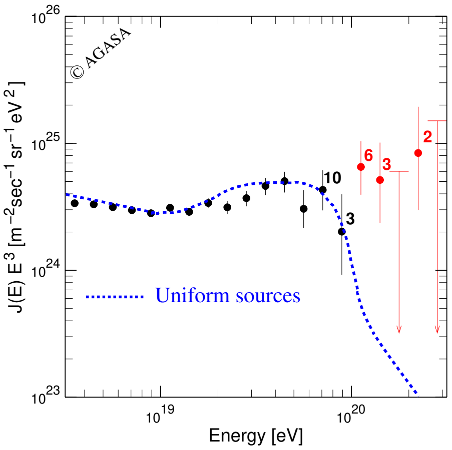

Figure 1.3: The AGASA energy spectrum multiplied by E^3. The error bars represent Poisson upper and lower limit at 68% and arrows are 90% C.L. The numbers attached to points show the number of events in each energy bin. The dashed curve represents the spectrum expected for extragalactic sources distributed unifomly in the Universe, taking account of the energy determination error

Recentely the experiment AGASA claimed to have detected cosmic rays with energy above 10^{20}eV (see figure 1.3), in clear contradiction with the limit set by the GZK cutoff. If confirmed, this particles of extremely high energy could be, for instance, the product of the annihilation of exotic supermassive “X” particles, radiated from topological defects formed during phase transitions as the early universe cooled. Since the predicted density of topological defects is very model-dependent, measurements on the high energy region of cosmic rays may impose constraints to the theories. On the other side, if their origin were a non exotic source, it should be very powerful and close enough to us so that the GZK cutoff would not prevent the particles to propagate until the Earth.

From this short overview it is clear that many questions are still open in CR physics. Precision measurements are necessary to improve the propagation models of cosmic rays and to tune their parameters. In next section we will discuss some detection techniques with some specific examples.

1.2 Cosmic ray detection

Maesurements of the CR flux in the Earth vicinity are affected by many factors. The most important is the solar modulation, which affects CR of low energy and has little influence on the energy range seen by AMS.

Another factor that affects CR trajectories near the Earth is the terrestrial geomagnetic cutoff. The magnetic field associated to the Earth can be approximated[4] by a dipole field, with magnetic poles shifted 11 degrees with respect to the geographic poles. Particles approaching the Earth undergo magnetic deflection depending on the field intensity and on their rigidity, and are guided by the field lines following trajectories determined by the field configuration. The dipole form of the field implies that there are permitted and forbidden zones to a particle coming from outside. Thus, for a particle arriving at a given point on the Earth surface one can compute a threshold energy below which the particle cannot reach the surface. This effect is called "geomagnetic cutoff" and some representative values for a particle arriving vertically are shown in table 1.1.

geomagnetic latitude (degrees)	cutoff rigidity (GV)
0	14.9
40	5.1
60	0.93

Table 1.1: Cutoff rigidity at different geomagnetic latitudes.

Stratospheric balloons are usually flown at high latitude in order to reduce this effect.

[4]the approximation holds within a 2–3 R_E, where $R_E = 6370$ km is the Earth radius.

Finally, CR arriving on top of the atmosphere ($\simeq$ 40 km above the sea level) interact with it, producing secondary particles. For this reason experiments aimed to perform direct measurements of CR have to be placed outside the atmosphere.

Very different techniques are used to measure the CR flux, depending on the energy range and on the expected rate. In the region below the knee it is possible to perform direct measurements of the charged particles and photons with experiments of limited dimensions outside the Earth atmosphere. For very high energy CR this task becomes more difficult because of the very low rate of particles. A more effective method consists in exploiting the interaction of high energy CR with the atmosphere and thus detect the products of their interaction with ground based detectors. This indirect measurement cannot provide the same precision, but can have very long duration and cover extended areas with no limitation due to the satellite or balloon constraints.

1.2.1 Direct measurement

In the energy range below the knee region the flux of CR is measured by direct detection of the particles.

Magnetic spectrometers are widely used for this purpose, typically in the energy range from 200 MeV up to 100–200 GeV; experiments on stratospheric balloons using emulsion chambers extend the energy range up to 1000 TeV, other experiments on satellite use different techniques like the multiple dE/dx-total energy loss, the double Čerenkov technique, or combined measurements from different detectors (for instance Cherenkov gas detector, scintillator counters and transition radiation detectors like CRN [46])

Magnetic spectrometers

Some examples are balloon borne experiments, like MASS2 [9], IMAX [30], ISOMAX [23], CAPRICE [11], BESS [33] and experiments designed to operate in space like AMS and PAMELA [44].

The method used by magnetic spectrometers to identify a particle is the magnetic rigidity versus velocity technique. A magnetic spectrometer consists essentially of a magnet of cylindrical shape, a tracking detector placed inside the magnet whose aim is to measure the particle track, and a time of flight system (TOF), made up by two or three planes of scintillator counters arranged just below and above the magnet.

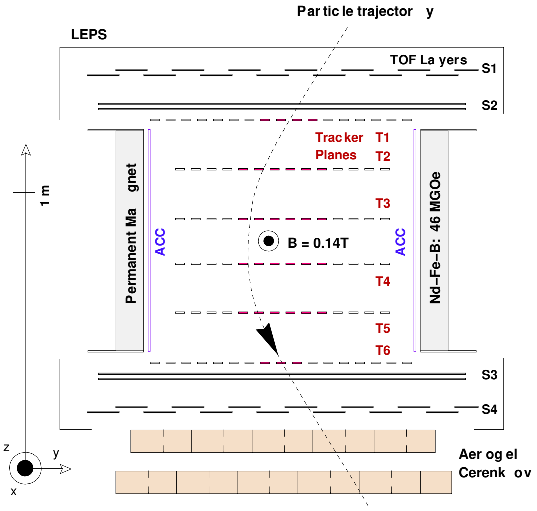

Figure 1.4: Section of a magnetic spectrometer (AMS-01) with a particle trajectory inside.

A charged particle which enters inside the detection volume of the spectrometer undergoes a deflection due to the Lorentz force $\vec{F} = q\vec{v} \times \vec{B}$, like illustrated in figure 1.4. The tracker measures different points along the particle path and gives a tridimensional reconstruction of the trajectory, then, given the value of the magnetic field, the rigidity of the particle can be determined. The velocity is measured by the TOF system: each plane gives a signal when the particle passes through it, thus the time of transit between the two planes is determined and, in turn, the velocity. The electric charge is measured from the energy loss in the material of the TOF or/and of the tracker. Finally the particle mass is determined using the relation:

$$m = \frac{RZ}{\gamma\beta} \tag{1.3}$$

where R is the rigidity, β is the particle velocity, Z its charge in electron charge units and γ the Lorentz factor.

Emulsion chambers

Another technique for direct measurement, widely used in the energy range 1-1000 TeV, consists in emulsion chambers [5] like JACEE [47] and RUN-JOB [39]. This technique, used by experiments on stratospheric balloons,

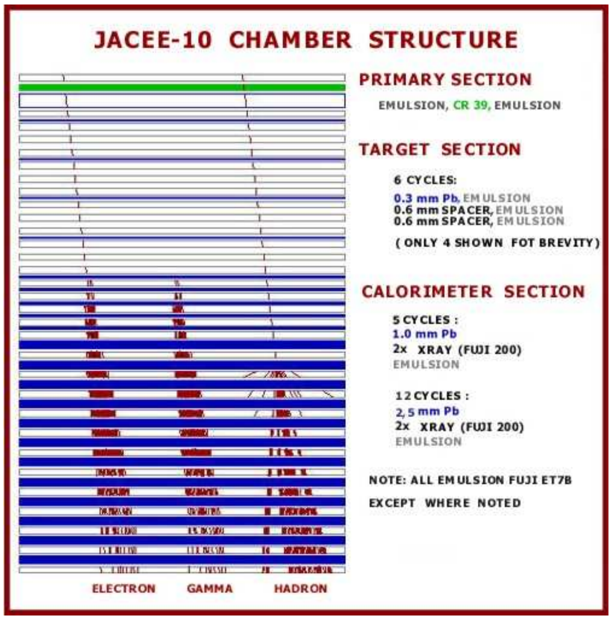

Figure 1.5: Display of a chamber of JACEE. Particles interact in the target section and their energy is measured in the calorimeter section.

allows the study of charge composition and energy spectra of primay CR. An emulsion chamber consists of a series of lead sheets alternated with emulsion plates and, in some detectors (like for example JACEE, as shown in figure 1.5) with X-ray films. A charged particle entering in the chamber suffers inelastic interactions in the lead producing many hadrons, especially charged and neutral pions. π^0 decay in $\gamma\gamma$ originating an electromagnetic cascade producing a shower of e^+/e^- and photons of bremstrahlung.

High energy photons and electrons cause dark spots in X-ray films. The cascade is then reconstructed along adjacent emulsion plates. By following

[5] Nuclear emulsions are special photographic emulsions with finer grain and additional sensitizers to record tracks of charged particles.

the cascade from plate to plate, one can study its development and reconstruct the interaction of the cosmic ray particles in the chamber. The absolute charge and energy of the primary particle can be determined.

Multiple dE/dx measurements

Another technique of direct detection consists in a series of measurements of the energy loss (dE/dx) combined with the total energy measurement. This approach is used, for instance, by the CRIS (Cosmic Rays Isotope Spectrometer) [16] aboard the ACE satellite, by the HET telescope on Ulysses and by the CRS instruments on the Voyager.

In figure 1.6 is shown a very schematic view of this kind of detector: various (in the figure only 2) solid-state detectors of known thickness arranged in a stack. A hodoscope reconstructs the particle trajectory and thus the angle θ. The energy loss, ΔE, in the first silicon detector can be approximated with the derivative, dE/dx, multiplied by the path length of the particle inside the material: $dE/dx \sim \Delta E \cos\theta/L$, using the Bethe-Block formula this quantity results to be proportional to Z^2/β^2.

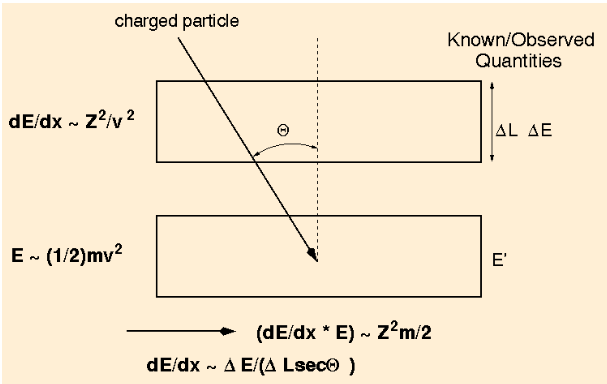

Figure 1.6: Display of the stack of a multiple dE/dx detector.

The energy, E', deposited in the second detector, where the particle comes at rest, is approximately the total energy of the particle: $E' = (1/2)mv^2$. Multiplying the two quantities one obtains:

$$E' * dE/dx \sim Z^2 m$$

For fully ionized particles, like CR, this quantity is sufficient to identify a nucleus.

With multiple measurements of dE/dx, using several stacked detectors, these experiments can achieve a mass resolution of ~ 0.25 amu up to Nickel (Z=28) and provide an excellent isotope separation (although in a limited energy range). Usually the energy range is limited by the requirement that the particle must be stopped in the last detector. Extending the energy range would imply a larger amount of material. The maximum energy reached by CRIS is 500 MeV/nucleon for nuclei in the Iron region, and $\sim$100 MeV/nucleon for light isotopes.

Double Čerenkov technique

In order to describe this technique, I will refer to the C2 telescope [19] which was flown on the HEAO-3 satellite in 1979. The detector consists of 5 Čerenkov counters with different radiators arranged in a vertical stack, each counter instrumented with 12 photomultipliers. A hodoscope of flash tubes is inserted between the counters, to determine the particle track parameters. The three inner Čerenkov counters have two different aerogel radiators and a teflon radiator with refractive index 1.012, 1.052, 1.33 respectively, and are used to determine the particle velocity. The two outer counters have radiators with higher refractive index and are used to determine the particle charge and momentum.

This experiment provided element identification up to Nickel, with a charge resolution ranging from 0.12 charge unit for $Z = 10$ (Ne) up to 0.20 for $Z = 26$ (Fe) in the energy range $0.6 < E < 35$ GeV. These data are usually taken as reference for the elemental abundancies and especially to study the B/C ratio in a wide energy range.

1.2.2 Indirect measurement

Other techniques have provided much information on the spectrum of high energy CR, typically extensive air shower experiments. These experiments are made up by arrays of ground based detectors sensitive to the products of atmospheric air showers. A schematic display of an extensive air shower (EAS) is shown in figure 1.7. A very important feature for these kind of experiments is the large extension: an EAS initiated by a cosmic ray of energy 10^{20} eV can cover a surface of 16 km^2 at ground level. For AGASA the extension of the whole experiment is of 100 km^2, for an experiment of the new generation, the Pierre Auger Cosmic Ray Observatory (now in construction in Argentina), the extension will be 3000 km^2. Over this surface only 30 particles of energy above 10^{20} are expected per year.

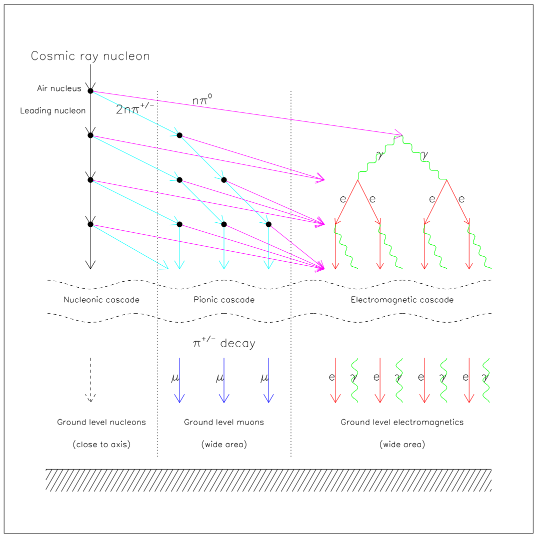

Figure 1.7: Display of the production of an atmospheric shower.

The traditional technique of detection used by these experiments consists in detecting the products of the EAS by means of an array of scintillator detectors. The shower reaching the ground hits simultaneously several detectors. Each hit detector sends a signal to a central data center which decides if the detected particles form a shower and, if this is the case, combines the measurements of the number of particles and their time of arrival at each station to reconstruct the direction and energy of the primary CR which initiated the cascade.

A second detection system is based on the detection of fluorescence light generated from the collision of the shower particles with air nitrogen molecules. The total amount of light is proportional to the number of particles in the shower and therefore to the energy of the mother particle, which can be determined with a resolution of about 10%.

The Auger Observatory will combine the two detection methods. It will have several fluorescence detectors that will be able to measure EAS in more detail than the giant array but can only observe fluorescence on moonless nights. Because the large surface array is active all the time, it measures 10 times more events. The surface array working in combination with the fluorescence detectors will make a powerful instrument for capturing and characterizing the rarest and most energetic cosmic rays.

The surface detectors of Auger should be able to distinguish if the particle that initiated the EAS is either a proton, a heavy nucleus, or a photon on the basis of the cascade longitudinal development and of the percentage of muons in the shower (the higher the muon percentage, the higher the atomic number of the nucleus that originated the EAS). This (partial) particle identification is of great importance, as the GZK cutoff is particle dependent[6], nevertheless, current uncertainties in hadronic interactions at such energies will limit the quality of the particle identification.

The problem of maximizing the detection surface is expected to be solved in an original way in the EUSO experiment [41]: the detector will look for the atmospheric cascades from space. From the International Space Station[7] EUSO will detect the fluorescence light emitted by atmospheric Nitrogen induced by the particles of the EAS produced by the primary CR. Using this technique the area seen by EUSO on the Earth surface will be about 160 000 km^2.

1.2.3 Conclusions

CR detection techniques are progressively improving both in ground based experiments and in experiments operated in space.

Direct experiments are trying to extend the upper limit of the accessible energy range and to improve the precision of their measurements. This objective is reached by means of the improvement of the detector sensitivity and of the extension of the experiments. Many collaborations perform several flights with the same detector (BESS, JACEE, RUNJOB etc).

On the other side the indirect experiments are trying to extend their surface, in order to collect more statistic of ultra high energy CR, and are exploring new techniques, like fluorescence light detection, to improve their sensitivity.

[6] the cutoff is 5×10^{19} eV for protons, but it is higher for heavier nuclei.

[7] the mission is foreseen to start in 2009 for a three operation period.

Chapter 2

The AMS experiment

2.1 Scientific goals

The Antimatter Magnetic Spectrometer (AMS) is a particle physics experiment designed to operate in space. Primary objectives of the experiment are the search for primordial antimatter components and for the annihilation products of dark matter in CR flux and to study antiprotons, positrons and light nuclei spectra [2].

2.1.1 Antimatter

The model of the hot Big Bang is the most reliable to explain the origin of the Universe for three main reasons: first, it accounts for the expansion of the Universe, discovered by Hubble as a recession of galaxies at a speed proportional to their distances from us: $v = Hd$ (H known as the Hubble constant); second, it can explain the abundance of light elements (He, D and Li) that were synthesized in the early Universe, when its temperature was high enough to produce them by nuclear fusion; third, it predicts a background radiation characterized by a very isotropic black body spectrum at a temperature of 3 K which is the echo of the decoupling of photons from matter, when the universe was cold enough to form neutral atoms (the CMB).

However, the absence of antimatter in the observed Universe is in disagreement with the hypothesis of an initial symmetry between matter and antimatter predicted by the hot Big Bang model. Measurements of the γ ray spectrum in the MeV region have shown no signal of the annihilation of a significant amount of matter-antimatter up to scale of the local supercluster of galaxies ($\simeq$ 30 Mpc). This means one of two possibilities: either the Big Bang somehow violated baryon number conservation and the initial antimatter was annihilated (or even never created), or the Big Bang did create matter and antimatter in the same quantity but during the evolution of the Universe matter and antimatter separated in different spatial domains, at scales larger than superclusters. Then, the Universe could be formed of domains of matter and antimatter and we see only matter because the Earth happens to be in a matter zone.

Following the hypothesis of an "all matter" universe, it is probable that the asymmetry between matter and antimatter originated at the end of the inflation, when baryons and antibaryons annihilated in different quantities and the leftovers of that process, known as *baryogenesis*, formed a universe of matter. Sakharov formulated the four conditions for baryogenesis to happen:

1. baryon number violation;
2. C violation;
3. CP violation;
4. a period out of equilibrium.

Of these requirements, the first has not been observed and proton decay experiments set the present limit of the proton lifetime to $t_p > 1.6 \times 10^{33}$ years [45]. The C violation in weak interactions was demonstrated in 1957 observing the different polarization state of e^+ and e^- in the decay of muons to electrons and anti-muons to positrons. The CP violation has been observed directly in the decay of the K_L meson since 1964, but with an amplitude much lower than necessary to produce cosmological baryon asymmetry. Finally the fourth condition is automatically satisfied in the Big Bang model. From these considerations we can conclude that the theory needed to support a baryonic asymmetric universe is still debatable.

On the other hand, the same Sakharov conditions offer the possibility for a baryonic symmetric universe, according to the scheme:

1. CP symmetry is spontaneously violated;
2. particles and antiparticles separate in different domains;

3. a period of inflation separate matter and antimatter domains to astronomical scale.

Following this scenario a baryonic symmetric universe is not ruled out.

To have an estimation of the size of the local matter domain, we can investigate the spectrum of gamma radiation coming from outer space. An abundant presence of antiprotons in cosmic rays would give a bump in the gamma ray spectrum, due to γ product of the decay of π^0 originated from antiproton annihilation with the ISM. The absence of such a signal puts limits on the relative abundance of antiprotons to protons. In the hypothesis of a mixed gas of protons and antiprotons we obtain these limits:

- $\bar{p}/p < 10^{-15}$ in the particle clouds in the Galaxy
- $\bar{p}/p < 10^{-10}$ in the halo of the Galaxy
- $\bar{p}/p < 10^{-5}$ in our cluster of galaxies

Direct search for antinuclei in cosmic rays is performed with detectors in stratospheric balloons or satellites. Antiprotons of secondary origin are known to be present in cosmic rays since 1958. Secondary antiprotons constitute a background for the detection of a possible cosmological component. This background has been measured [6] and decreases at energies above 10 GeV, thus antiprotons detected at much higher energy could be of cosmological origin.

For what concerns anti-nuclei, up to date balloon borne experiments have set upper limits to their abundance in primary cosmic rays (see figure 2.1). From these measurements we know that the flux of $\overline{He}$ or $\overline{C}$ (if exists) should be a very faint signal. Observation programs are pointing to increase the statistics by long duration experiments and to improve the sensitivity and particle identification capability of the detectors.

2.1.2 Dark Matter

Several independent astronomical observations based on clusters of galaxies, gravitational lensing, cosmic flows and power spectra of galaxies, point to an average density of matter in the Universe of about $0.2 < \Omega_m < 0.4$ [1][37] [34].

[1] Ω_m is the matter density normalised to the the critical density, ρ_c: $\Omega_m = \rho_m/\rho_c$; ρ_c is the matter density required to make the Universe closed: $\rho_c = 1.88 \times 10^{-29} H^2 gcm^{-3}$ where H is the Hubble constant.

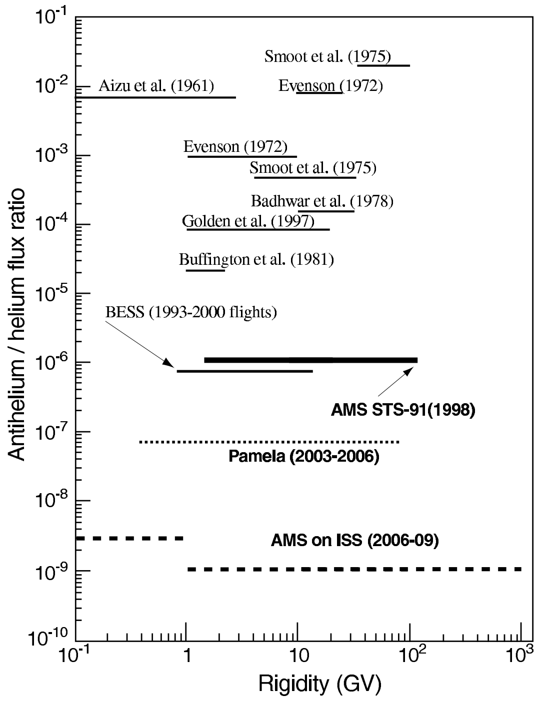

Figure 2.1: Limits to anti-nuclei in primary cosmic rays set by previous experiments.

The measurement recently obtained by the WMAP experiment [10] for this quantity ($\Omega_m = 0.27^{\pm 0.04}_{\pm 0.04}$) has a much better precision and is consistent with previous estimations.

The contribution to the overall matter density due to luminous matter is only about $\Omega_l = 0.003$, that is, most of the matter is non luminous, or dark. The most direct evidence for dark matter is provided by the observation of the rotation curves of spiral galaxies. The orbital velocity rises linearly from the center outwards, up to a value of 200 km/s, and then remains flat. This observation is completely unexpected, since the luminosity of the disk falls off exponentially, suggesting that most of the matter forming the galaxy is concentrated in the central bulge.

In addition, from the theory of primordial nucleosinthesis, the contribution of baryonic matter to the total matter content of the Universe is only $\Omega_b \simeq 0.05$. From these considerations we conclude that most of the matter in the Universe is dark and that most of it is non baryonic.

The first candidate for non baryonic dark matter is a massive neutrino, for its great abundance in the Universe and for its low cross section that makes it almost “invisible”. Recently, neutrino oscillation experiments have established that neutrinos do have a mass, but its value is still unknown, The limit set by tritium decay experiment of $m_\nu < 2.2eV$ puts a limit $\Omega_\nu < 0.14$ to the contribution of neutrinos to the non baryonic dark matter. A limited contribution of neutrinos to the Universe matter density was not unexpected. The evolution theory from the primordial fluctuations to the large scale structures (bottom-up) observed in the present Universe indicates that most of the non baryonic dark matter is cold, that is massive particles with negligeable thermal velocity in the early Universe. These theories of Cold Dark Matter (CDM) are currently the most successful in explaining the formation of all the structures (spatial distribution of galaxies, number density etc..) we see in the universe today, in good agreement with data. These theories set a further limit to the contribution of hot dark matter (that is neutrinos) of $\Omega_\nu < 0.05$.

From different arguments, it is clear that neutrino is only a subdominant component of non baryonic dark matter. So the next candidate is a massive (therefore no relativistic) weak interacting particle (the so called “WIMP”). To identify a WIMP with a specific particle it is necessary to move beyond the Standard Model. Altough no experimental evidence has supported it, Supersymmetry (SUSY) seems the natural extension of the SM, necessary to unify gravity with the other fundamental forces. The lightest particle predicted by SUSY, the neutralino (χ), is a good candidate for a WIMP.

According to CDM models, galaxy formation starts with a cold dark matter halo, and then the gravitational collapse of baryons gives rise to the luminous component. If WIMPs are relics of those primordial halos, we expect to find them in the dark halos of current galaxies. In accordance with SUSY models, WIMP annihilations generate quarks, leptons, gauge bosons and Higgs bosons, which in turn decay into stable particles that we can detect in cosmic rays.

The experimental search for neutralinos is performed via direct measurement for interaction of the neutralino with ordinary matter, or with indirect methods, looking for the products of $\chi - \chi$ annihilation in the galactic halo. This latter hypothesis opens the possibility to search for some signal of its annihilation in rare cosmic rays; stable cosmic rays species generated in neutralino annihilation include: γ rays, positrons, neutrinos, antiprotons and antideuterium, and in the same quantity their antiparticles. The indirect search

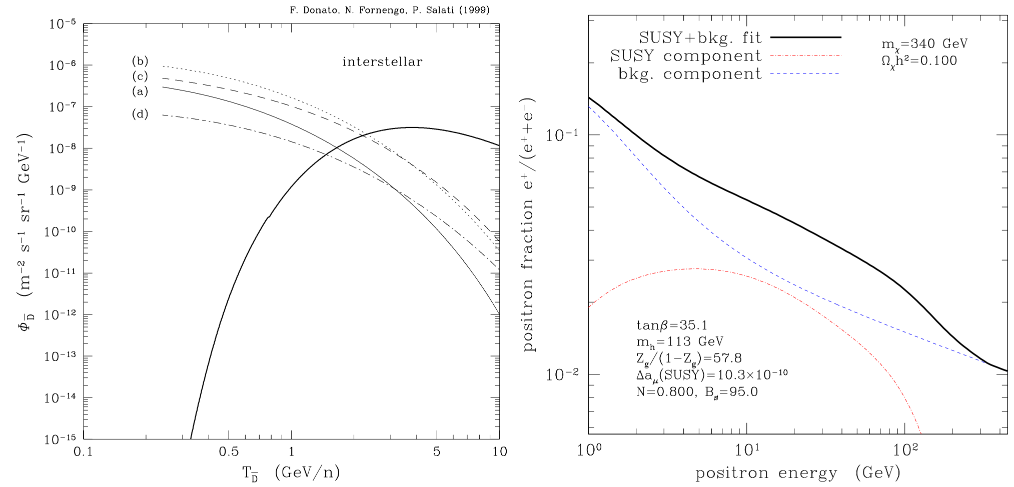

Figure 2.2: Left panel: $\overline{D}$ flux from secondary production (continuous line) and from different supersymmetric models (dashed lines) discussed in [40]. Right panel: predicted e^+ flux from the SUSY component (red curve), from the background (blue curve) and the total flux (black continuous curve).

is focused on γ rays and antiparticles, as in these cases the background from standard sources is scarce. The expected signature of neutralino annihilation in the different cases is described in the following [49]:

- $\bar{p}$: Currently, calculations of $\bar{p}$ spectrum of secondary origin are quite accurate and give a spectrum very flat for E<1GeV, as the $\bar{p}$ in the secondary reaction reactions are produced with non zero momentum. This suppression at low kinetic energy is not predicted for $\bar{p}$ coming from neutralino annihilation, thus an excess in the flux of antiprotons at low energy could be a possible signature. Very accurate experiments would be necessary to discriminate such a signal from the background of secondary antiprotons.

- $\bar{D}$: The flux of antideuterium from the merging of $\bar{p}$ and $\bar{n}$ (both product of $\chi - \chi$ annihilation) is expected to be 4 orders of magnitude smaller than the antiproton flux; nevertheless the ratio signal/background could be greater than that of antiprotons ($\bar{D}$ is very scarcely produced in cosmic rays spallation). In figure 2.2, left panel, is shown the flux of antideuterium predicted by some supersymmetric theories [40].

- e^+: Positrons coming from the annihilation of neutralinos should give an excess of signal in the region around the neutralino mass. In figure 2.2, right panel, is shown the expected positron fraction.

- $\gamma\gamma$: As WIMP move in the Galaxy at no relativistic velocity, the photons coming from its annihilation are nearly monochromatic, with energy near to the neutralino mass. In figure 2.3 is shown the gamma diffuse background and the signal expected for two different values of m_χ.

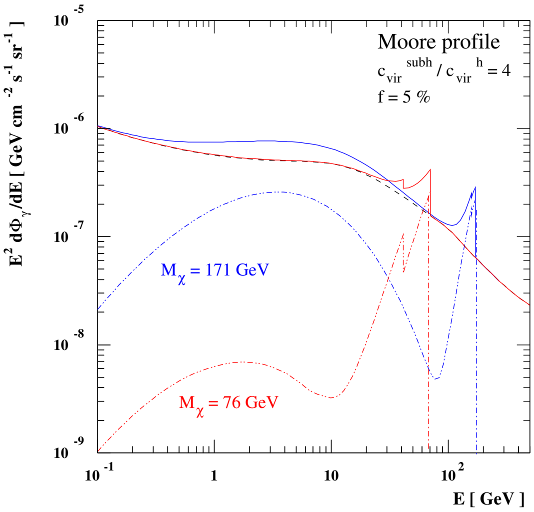

Figure 2.3: Gamma ray diffuse background and signals predicted for different values of m_χ.

From all these considerations we can conclude that search for antimatter and dark matter requires an experiment with large geometrical acceptance and long duration of the exposure in order to collect a large amount of data; these characteristics together with a good particle identification capability enable the detector to search for very faint signals in the cosmic rays flux.

This is the objective of the AMS experiment and in the next paragraphs we will illustrate how the detector is structured, and which are the expected performances.

2.2 AMS-01

The first mission of the experiment consisted in a ten day flight onboard the shuttle Discovery, in june 1998. The mission was very useful to the collaboration to gain experience with space tecnology and to gather information on particles rates, effect of the geomagnetic cutoff on particle trajectory, detector thermal control and general detector operation [3]. The detector was composed by: a permanent magnet of bending power BL^2=0.15 Tm^2, a fraction of the silicon tracker that will be used for AMS-02, a time of flight system of four planes (two above and two below the magnet), an anticoincidence counter and a Čerenkov threshold counter. Altough the detector was not optimized for lepton/hadron separation at high energy or to measure low energy antiprotons, a large amount of data (100 millions triggers) was collected. The measurements cover all geographic longitudes and most latitudes (from -51.6^o to 51.6^o) and allow an accurate measurement of cosmic ray spectra and also a systematic study of the effect of geomagnetic field on the low energy region of the spectra. In summary the main results of AMS01 are:

- no anti-helium was detected at any rigidity. The upper limit to the ratio $\overline{He}/He$ has been set to 1.1×10^{-6} in the rigidity range 1–140 GV with 95% confidence level;
- proton and helium flux has been measured from 0.2 GeV to 140 GeV with high statistics (see table 2.1);
- e^- and e^+ spectra have been measured in the energy range 0.2–20 GeV and 0.2–2 GeV respectively;
- In addition to the primary spectrum, these results have shown the existence of a second spectrum of particles with energy below the geomagnetic cutoff. These particles cannot come from outer space as they are in forbidden orbits. They are originated by interactions of primary cosmic rays with the upper layers of the atmosphere.

2.3 AMS-02

The AMS collaboration is now working on the detector for the second mission of the experiment. In 2005 an upgraded detector, AMS–02, will be ready

proton flux	
γ	2.78$\pm$ 0.009(fit) $\pm$ 0.019 (syst)
Φ_0	17.1 $\pm$ 0.15(fit)$\pm$1.3 (syst)$\pm$1.5(γ)GV$^{2.78}$($m^2 s\, sr MeV$)
helium flux	
γ	2.74$\pm$ 0.010(fit) $\pm$ 0.016 (syst)
Φ_0	2.52 $\pm$ 0.09(fit)$\pm$0.13 (syst) $\pm$0.14(γ)GV$^{2.78}$($m^2 s\, sr MeV$)

Table 2.1: Results of the fit of the proton and helium spectrum with a power low $\Phi = \Phi_0 R^{-\gamma}$ in the range $10 < R < 200$ GV.

for a three-year mission on the International Space Station. The main improvements with respect to the AMS–01 instrument consist of the increased magnet bending power (from 0.15 of the permanent magnet of AMS-01 to 0.86 Tm^2 of the new superconducting magnet), the inclusion of a transition radiation detector, an electromagnetic calorimeter and a ring imaging Čerenkov detector, that will make possible particle identification in a much wider energy range, especially lepton/hadron discrimination.

The total weight of the detector is about 6 tons, and the total power available for the experiment 2 kW. The detector AMS-02 is shown in figure 2.4; in next sections all its subdetectors will be described [14].

2.3.1 The magnet

The main body of the detector consists in a superconducting magnet of 1.2 m of inner diameter, made up by 2 main dipole coils and 12 racetracks coils, refrigerated by a circuit of liquid helium at 1.8 K. The field provided by the magnet is very intense and uniform with direction perpendicular to the cilinder axis. The bending power is 0.86 Tm^2 and the stray field outside the magnet falls off very rapidly. The weight of the magnet is about 2.3 tons. A layer of plastic scintillators covers the internal surface of the magnet to veto stray trajectories and secondary particles produced in the magnet.

2.3.2 The Time of Flight (TOF)

The TOF provides the fast trigger to the experiment, a measurement of the charge and of the velocity with a precision of about 3%. It also discriminates the direction of the incoming particle (up-down or vice versa) with sensitivity 10^{-8}. This direction, combined with the track curvature provided by the tracker, determines the charge sign of the particle. The charge measurement is based on the energy deposited in the paddles by ionization and/or excitation, expressed by the Bethe–Block formula [26], which is proportional to the charge squared: $-dE/dx \propto Z^2/\beta^2$.

This detector consists of four plastic scintillator planes (two above and two below the magnet). Each plane consists of 11 cm wide paddles. The light produced in the paddles is collected, through light guides, by two photomultipliers present at each end.

2.3.3 The Silicon Tracker (SI)

This detector is designed to perform high precision measurement of the particle rigidity and charge value. It is based on eight thin planes of double–sided silicon microstrip detectors placed inside the magnet, which will provide a spatial resolution better than 10 μm in the bending direction and 30 μm in the non bending. For protons the momentum resolution is expected to be $\sim 1.5\%$ at 10 GeV. In addition to this, the tracker can determine the charge of the particle form the energy deposited in the paddles, just like the TOF.

2.3.4 The Electromagnetic Calorimeter (ECAL)

The aim of this detector is to extend electron/hadron separation up to 1 TeV, with a discrimination factor of $\sim 10^{-4}$. Furthermore the ECAL will provide high energy γ detection (above 10 GeV) with good angular and energy resolution.

The ECAL is placed just below the RICH, and consists of 9 scintillating fibers superlayers, with a total radiation length of $15\% X_0$. Each superlayer consists of ten layers of lead planes with one mm scintillating fibers glued in between.

2.3.5 The Transition Radiation Detector (TRD)

The TRD is made up by 20 layers of straw tube modules and propylene fibers radiators. The straw tubes, operated at high voltage with a mixture of Xe and CO_2, detect the transition radiation generated by ultra-relativistic particles and provide additional points for tracking. The TRD will be sensitive to $e^{\pm}$ and γ that convert in a pair e^+e^- interacting in the detector material. Covering the whole geometrical acceptance of the magnet the TRD will separate electrons from protons up to 300 GeV with a rejection factor of $10^2 - 10^3$.

2.3.6 The Ring Imaging Čerenkov detector (RICH)

Instead of the threshold Čerenkov detector of AMS01, a RICH detector will be placed below the last plane of the TOF. Its aim is to measure particle velocity and charge, as will be explained more in detail in next chapter.

2.3.7 Expected performances

The expected performances of AMS–02 after three years of data taking on the ISS are summarized in table 2.2. The most relevant issue is that the $\overline{He}/He$ limit will be improved of three orders of magnitudes with respect to the current value.

Another very important goal of AMS is to extend the energy range of antiproton measurements form 50 GeV (measurements of the MASS91 [8] and CAPRICE98 [12] experiments) up to 300 GeV. The total number of collected $\overline{p}$ will be 5×10^5.

Measurement	sensitivity or statistics	energy range	physics
e^+	10^8	0.1–300 GV	
$\overline{p}$	5×10^5	0.5–300 GV	Dark matter
γ ray	10^4	1–10^3 GeV	
$\overline{He}/He$	10^{-9}	0.5–10^3 GV	Antimatter
$\overline{C}/C$	10^{-8}	0.5–10^3 GV	
D	10^9	0.1–10 GeV/A	
^3He	10^9	0.1–10 GeV/A	Astrophysics
^{10}Be	10^5	1–10 GeV/A	

Table 2.2: Expected capabilities for AMS-02 after three years on the ISS.

For what concerns isotope identification, AMS will collect a huge amount of D, ^{3}He and ^{10}Be and will extend significantly the energy range of isotope separation; for instance ^{10}Be identification is expected to be extended up to 10 GeV/n.

Finally, a very interesting issue of the detector is the possibility of γ ray measurement in the range 1–300 GeV. A γ ray inside the TRD interacts with its material and converts in a pair e^+e^-. The identification and reconstruction in the tracker of the two charged particles allow to determine the primary γ energy with a resolution of $\simeq 2\%$, and its direction with an angular resolution of better than 0.03^o at energy $E \geq 10$ GeV. In addition to this, the ECAL will measure in stand-alone mode γ-rays that have not interacted in the upper material of the detector.

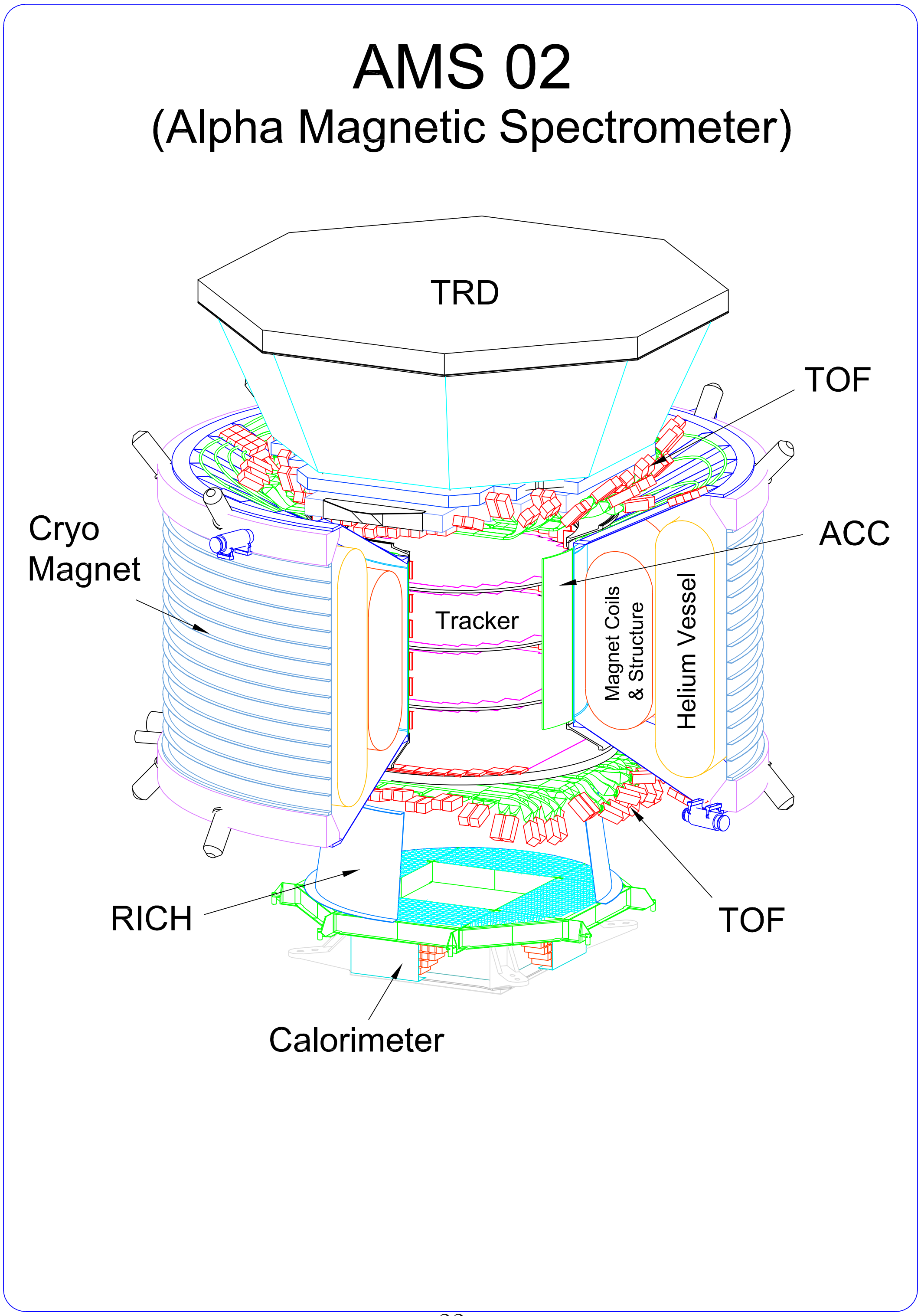

Figure 2.4: AMS-02 detector layout.

Chapter 3

The RICH detector of AMS–02

For its second mission the AMS experiment will be equipped with a RICH detector to extend particle identification to higher momentum.

RICH counters are based on the detection of Čerenkov light produced by charged particles. The Čerenkov effect has been widely used to perform particle identification in high energy physics experiments.

In this chapter a general introduction on Čerenkov detectors will be presented [42]; then the Čerenkov threshold detector of AMS-01 will be briefly described and its substitution in the second mission with a RICH detector will be justified. Finally the RICH of AMS-02 is presented.

3.1 Čerenkov light emission

When charged particles pass through a dielectric material they induce the creation of atomic dipoles. If the velocity of the particles is greater than that of light in the medium (i.e. $v > c/n$) the variation with time of the induced dipolar moments will originate the emission of electromagnetic radiation, called Čerenkov radiation. By simple geometrical arguments (see figure 3.1) it is easy to see that the emitted photons will form an angle θ_c with respect to the velocity of the particle given by:

$$\cos\theta_c = \frac{ct/n}{vt} = \frac{1}{n\beta} \tag{3.1}$$

and the azimuthal angle is uniform in $[0, 2\pi]$.

The number of emitted photons can be expressed in natural units as

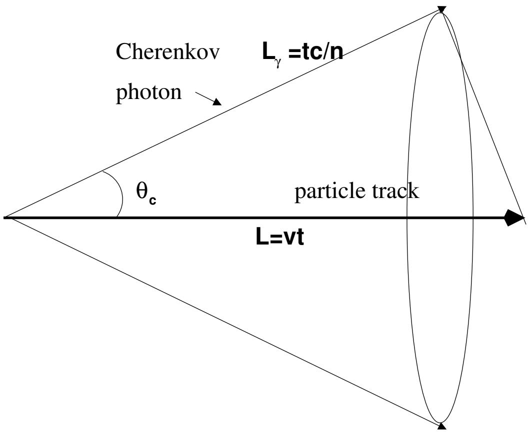

Figure 3.1: Display of Čerenkov light emission.

$$dN/d\omega = \alpha z^2 L sin^2\theta_c \tag{3.2}$$

where L is the pathlength inside the radiator, α is the fine structure constant, z the particle charge and $\omega(E)$ the energy of the photon. From equation 3.1, it is clear that

$$sin^2\theta_c = 1 - 1/(n\beta)^2$$

The refractive index depends on ω, $n = n(\omega)$, however, if the material is not very dispersive, we can consider that in the optical region of frecuencies n is almost independent of ω and therefore:

$$N = N_0 z^2 L sin^2\theta_c \tag{3.3}$$

where N_0 is usually called *response parameter* of the detector [51], and is expressed by the relation:

$$N_0 = \alpha\epsilon\Delta E \tag{3.4}$$

and ϵ is the mean efficiency calculated over the energy interval $\Delta E = E_{max} - E_{min}$:

$$\epsilon\Delta E = \int (QTR) dE \tag{3.5}$$

In the previous equation Q is the quantum efficiency of the photodetector which has to convert Čerenkov photons into electrons, T is the transmittance of the different media which compose the detector (usually the radiator, and the vacuum where photons propagate), and R is the reflectivity of the mirror[1], which is used to focus the photons. N_0 is a parameter which characterizes the goodness of a detector as it is proportional to the number of photoelectrons detected with a radiator of unit length. The dependence of the spectrum on the squared charge of the particle allows the identification of different nuclei.

3.2 Classification of Čerenkov counters

Čerenkov light finds many applications in experimental physics. In this section some Čerenkov detectors for high energy particle measurements are discussed.

3.2.1 Differential counters

In differential counters photons are focused by a lens which refracts them to the photodetector system. This class of detectors can reach very good β resolution (of order of $\sigma_\beta/\beta \simeq 10^{-6}$), however its acceptance in phase space[2] is very limited because, by construction, they can only focus photons emitted at a given angle, and this means measuring particles of a given β, and a given direction.

3.2.2 Threshold counters

The Čerenkov threshold counters are detectors which give a signal when a particle above threshold crosses them. This type of detectors do not have to measure the Čerenkov angle of photons, they simply detect photons and convert them in an electric signal whose amplitude is related to the velocity and charge of the particle (from equation 3.3, $N \sim 1 - 1/(n\beta)^2$). This allows the measurement of β in a wider kinematic range ($\Delta\beta = 1 - 1/n$) than a

[1]if there is no mirror, this factor is ignored.

[2]we call phase space the space (β, θ_p), where β is the particle velocity and θ_p its direction. The acceptance in this space is A=KS$\Delta\Omega\Delta$p, where K is a normalisation constant, S the photodetector surface, Ω the solid angle, Δp the momentum acceptance.

differential counter, but with a poorer resolution. If N is the number of detected photoelectrons then, from equation 3.2, we have that

$$\frac{\sigma_N}{N} = \frac{1}{\sqrt{N}} = 2cotg\theta_c\sigma_\theta \tag{3.6}$$

In order to obtain the β resolution we can write:

$$\frac{\sigma_\beta}{\beta} = tg\theta\sigma_\theta \tag{3.7}$$

which results from $\theta_c = acos(1/n\beta)$. Combining equations 3.6 and 3.7 we have the limiting β resolution is:

$$\frac{\sigma_\beta}{\beta} = \frac{tg^2\theta}{2\sqrt{N}} \tag{3.8}$$

If the mean number of photons is large, threshold counters can provide a good β resolution (up to $\sigma_\beta/\beta \sim 10^{-5}$) but with a large phase space acceptance.

3.3 RICH counters

The RICH technique couples good phase space acceptance and high β resolution, by measuring the ring image which is formed by the radiated photons. RICH detectors have been developped and improved during the last 40 years and nowadays they provide the most accurate measurement of the velocity of ultrarelativistic charged particles. There are two main classes of RICH detectors: with focusing mirror, and without it (*proximity focusing* RICH detectors). In any case, the basic idea is to form a ring image on a photodetector surface, in order to geometrically reconstruct the light cone and, in turn, compute the Čerenkov angle.

3.3.1 Velocity resolution

From equation 3.7, the estimated uncertainty on β for N detected photoelectrons can be expressed as:

$$\frac{\sigma_\beta}{\beta} = \frac{\sigma_\theta tg\theta}{\sqrt{N}} \tag{3.9}$$

where σ_θ is the total angular error per detected photon. This formula suggests that the resolution per single photoelectron improves for small Čerenkov angles, and thus small refractive index, which is a general rule for Čerenkov detectors.

Moreover, formula 3.9 shows that the β resolution for a RICH counter depends explicitely on the error of the Čerenkov angle, while in formula 3.8 σ_θ does not appear, because in threshold counters the β is measured by the pulse amplitude of the signal. If we compare the β resolution obtained with the two techniques:

$$\frac{(\frac{\sigma_\beta}{\beta})_{\mathrm{RICH}}}{(\frac{\sigma_\beta}{\beta})_{\mathrm{THRESH}}} = \frac{2\sigma_\theta}{tg\theta} \tag{3.10}$$

The ratio σ_θ/θ can reach values of order of 10^{-3}, so the determination of β from a measurement of the Čerenkov angle is more precise than from the measurement of the intensity of the signal, i.e. the number of photoelectrons. This happens because the number of photoelectrons is usually quite low and suffers very large statistical fluctuations, while the angle does not, and only depends on β and n.

The uncertainty on the Čerenkov angle is given by the sum in quadrature of all the possible sources of error.

The physical quantities one has to measure in order to find θ_c are:

- particle direction (θ_p, ϕ_p)
- photon detection coordinates on the photodetector surface
- the chromatic dispersion of the radiator

The particle direction is not measured by the RICH. An external tracker detector must provide the particle direction and impact point on top of the radiator, thus on this detector sensitivity depends the precision of θ_p and ϕ_p.

The photon detection coordinates precision depends on the position resolution provided by the RICH photodetection system. For this reason the phtotodetectors must have an adecuate position resolution in order not to compromise the global precision of the measurement.

Chromatic dispersion of the radiator represents an intrinsic source of uncertainty:

$$\sigma_\theta(E) \propto \left(\frac{dn}{dE}\right) \Delta E$$

This error can be reduced only by limiting the energy bandwith, ΔE.

Finally, the photon emission coordinates inside the radiator, for proximity focusing detectors, have an irreducible error which can only be reduced by minimizing the radiatior thickness. For RICH with a focalisation system, this source of error does not exist, as all the photons are focalised to the same point.

3.4 AMS-01 threshold Čerenkov detector

As explained in section 2.2, the prototype detector of AMS was equipped with an Areogel Threshold Čerenkov counter (ATC), to discriminate antiprotons from electrons and positrons from the huge proton background (in primary CR the relative abundancies are: $\bar{p}/e^- \simeq 10^{-2}$ and $e^+/p \simeq 10^{-3}$).

The elementary component of the ATC is the aerogel cell, of size $11\times11\times8.8$ cm^3, filled with eight 1.1 cm thick aerogel blocks [29]. For each cell a light guide collects the emitted light onto a photomultiplier. The 168 cells are arranged in two layers.

The aerogel refractive index is n=1.034, resulting in a threshold for light emission β_t=0.967, which corresponds to a momentum of threshold of $\simeq$2 MeV for positrons and electrons and 3.57 GeV for protons and antiprotons. The ATC allowed to extend the positron/proton separation up to 3.5 GeV, with a rejection factor of 260, and efficiency of 41%, and electron/antiproton separation with rejection factor 330 and efficiency 48%.

In the second phase of the experiment, the ATC will be substituted by a RICH detector which will provide a precise β determination. In next section a detailed description of the RICH will be given.

3.5 AMS-02 RICH

3.5.1 The role of the RICH in AMS-02

As explained in section 1.2.1, the mass of a particle can be determined from the independent measurement of its momentum, p, and velocity. The mass resolution is given by:

$$\left(\frac{\Delta m}{m}\right)^2 = \gamma^4 \left(\frac{\Delta\beta}{\beta}\right)^2 + \left(\frac{\Delta p}{p}\right)^2 \tag{3.11}$$

from equation 3.11 it is clear that the total error on m is dominated by the β resolution, $\Delta\beta$, which is amplified by a factor γ^2. In AMS-01 the particle velocity was determined with the TOF system. Using this technique $\Delta\beta$ is directly related to the time resolution of the TOF, Δt:

$$\frac{\Delta\beta}{\beta} = \frac{\Delta t}{t} = \frac{\Delta t}{L}\beta c \tag{3.12}$$

where L is the distance between the TOF planes. For a flight distance of 1 m and a time sensitivity of 120 ps the β resolution is $\Delta\beta/\beta = 3\times10^{-2}\beta \simeq 3\%$ for relativistic particles. A similar value of time resolution will be provided by the TOF system of AMS02.

If the momentum resolution provided by the AMS tracker is 2%[3] and one substitutes these values of $\Delta\beta$ and Δp in equation 3.11 it is evident that the total error on the mass is dominated by $\Delta\beta$. In order to have a total error Δm comparable with the error on the momentum it is necessary to have a β measurement with an error at level of 0.1%. As shown in figure 3.2, the precision $\Delta m \sim \Delta p$ is obtained up to $\gamma \sim 4-5$.

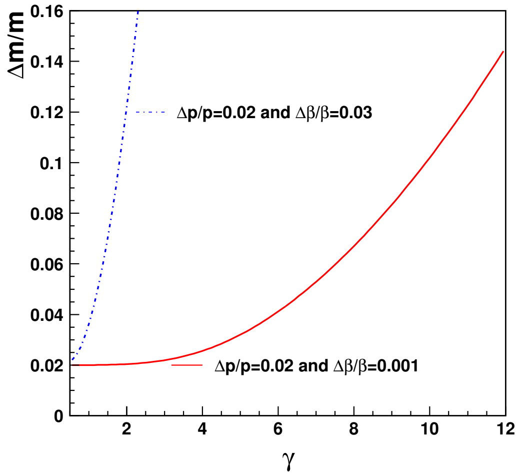

Figure 3.2: Mass resolution versus Lorentz factor, γ, for different values of β resolution.

For this reason the AMS–02 spectrometer will be provided with a RICH detector which will measure β with a precision of 0.1% for $Z = 1$ particles and

[3]this is the expected value of momentum resolution for a proton of 10 GeV.

will be able to separate isotopes of Helium and Beryllium up to 10 GeV/n. In addition to this, the wide dynamic range of photomultipliers+electronics of the RICH will allow charge measurement in a more extended Z range with respect to solid state detectors.

3.5.2 Description

The AMS-RICH (see figure 3.3) consists of a layer of radiator, a conical mirror and a photodetector plane, made up by an array of 680 photomultipliers (PMTs).

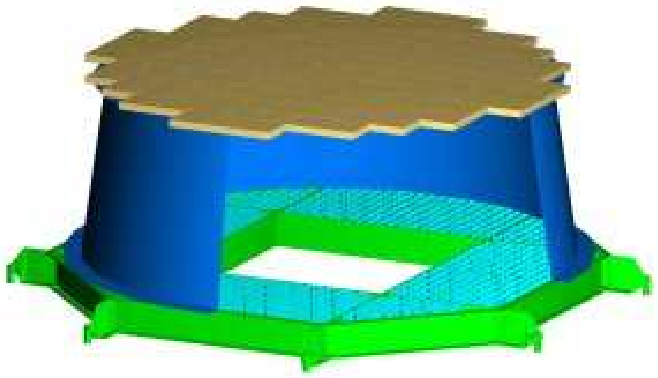

Figure 3.3: Sketch of the AMS–02 RICH: the radiator layer is placed on top of the conical mirror; below it the PMT matrix with the support structure are visible.

The conical mirror encloses the expansion volume, of 47 cm height, between the radiator and the photodetection plane and, thanks to its high reflectivity (R =0.85), increases significanlty the number of collected photons. Its upper circumference, of 60 cm radius, is fixed to the grid which supports the radiator blocks. The bottom circumference has radius 67 cm and delimits the photodetection area. The RICH is placed just below the last TOF plane and above the ECAL, and has an acceptance equal to the 80% of the magnet. In the central part of the detection plane a square region of side 63 cm is not instrumented to avoid interactions before the calorimeter.

The total dimension of the detector are 1.2 m and 1.34 m top and bottom diameter respectively, and 0.6 m height. The total weight is 184 kg and the power consuption is 110 W.

Radiator material

The radiator is a fundamental component of a Čerenkov detector since the kinematic range and the velocity resolution strongly depend on its optical properties.

The AMS RICH proposed configuration consists in a mixed radiator of silica aerogel and of sodium fluoride (NaF). The radiator tiles (blocks of 11×11×3 cm^3 of aerogel and 8.5×8.5×0.5 cm^3 of NaF) are arranged in order to cover the upper section of the mirror, as shown in figure 3.3. The radiator blocks are supported by a plastic foil, and cover a total surface of about 3600 cm^2.

The Čerenkov cone produced in the NaF has a large opening angle. Therefore this material has been used in the central zone (34×34 cm^2) to improve the reconstruction efficiency and to enlarge the kinematic range towards lower energies.

Sodium fluoride: Sodium fluoride is a crystal of refractive index 1.33 (see figure 3.4, left panel), so the threshold for Čerenkov light emission is $\beta_{th} = 0.76$. Because of its high refractive index, the expected β resolution in the AMS-RICH configuration is $\sigma(\beta) \simeq 3 \times 10^{-3}$, and has the advantage of extending the kinematic range down to 1.1 GeV/c for protons(antiprotons). This crystal has the lowest refractive index of all common optical materials and high transparency to UV light (see figure 3.4 right panel); these characteristics makes it of great interest for Čerenkov detectors.

Silica Aerogel: The radiator covering most of the acceptance of the AMS RICH consists of silica aerogel. Traditional gas radiators have refractive index lower than 1.0018 (C_5F_{12}) and liquid radiators higer than 1.27 (liquid C_5F_{12}). The only material which can partially fill the gap between these values is silica aerogel, which can be produced with a refractive index ranging from 1.004 to 1.1. Aerogel is a mixture of grains of amorphous SiO_2 and air. The relative quantity of SiO_2 and air can be adjusted in order to get the desired density and refractive index. The relation between refractive index, n, and density, ρ (in g/cm^3) of the resulting material is expressed by [28]:

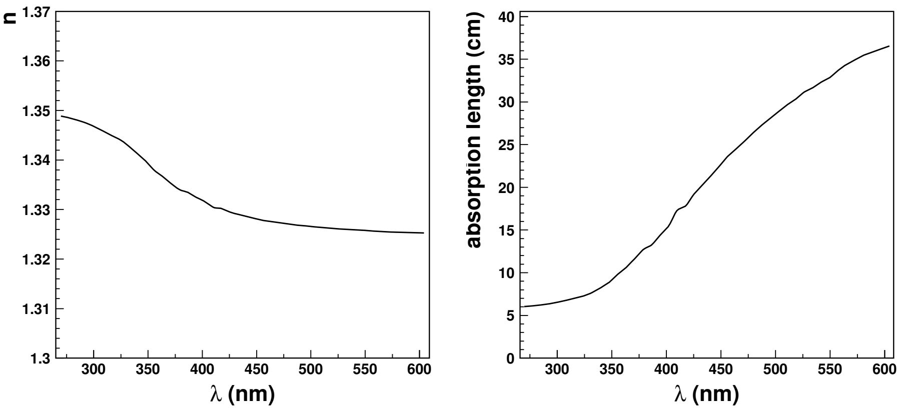

Figure 3.4: a) Refractive index versus photon wavelength and b) absorption length for sodium fluoride.

$$\rho = (n - 1)/0.28 \tag{3.13}$$

Aerogel is a material produced through a quite complicated process. The first phase is the hydrolysis of silicon oxides in a solvent, later the solvent must be removed without evaporate, and this requires a very good control of temperature and pressure conditions. The final solid sample is obtained with a drying procedure.

Optical properties of aerogel are determined by its granular structure, tipycally of few nanometers. Visible light which passes through this medium can be dispersed by these pores and undergo Rayleigh scattering. This phenomenon is the major drawback of aerogel for RICH detectors, because it determines the loss of part of the Čerenkov photons produced. The transmittance of a sample of aerogel is expressed by:

$$t(\lambda) \propto Ae^{-xC/\lambda^4}$$

were λ is the wavelength of the photon, x is the path length of the photon inside the aerogel, A is a constant depending on the material and C is a parameter characteristic of the material, called *clarity*, usually expressed in units of $\mu m^4/cm$. The optimum optical properties are thus fulfilled for $A \sim 1$ and $C \sim 0$.

All the results shown in chapter 4 are relative to an aerogel with a nominal refractive index $n = 1.05$, which provides a velocity threshold $\beta_{th} = 0.97$ and a β resolution at level of 0.1% for $Z = 1$ particles. Nevertheless the aerogel for the final RICH design is still under evaluation. Precise measurements of transmittance of aerogel samples with index $1.03 < n < 1.05$ are currently in progress at CIEMAT.

Photon detection

Light detection in AMS-RICH is performed by an array of 680 Hamamatsu PMTs R7600-00-M16 [22]. This phototube has been chosen on the basis of the requirements imposed by the AMS experiment and for the specific needs of the RICH detector.

Space operation sets strict constraints on weight and power consumption and requires devices which can stand to temperature variations, vibrations and low pressure. On the other hand, the specific needs of the AMS-RICH require a PMT with high photon efficiency and good spatial resolution to allow a precise reconstruction of the Čerenkov ring. Other important features are a good single photoelectron (s.p.e.) resolution and linearity in the response to perform photon counting needed for charge measurement.

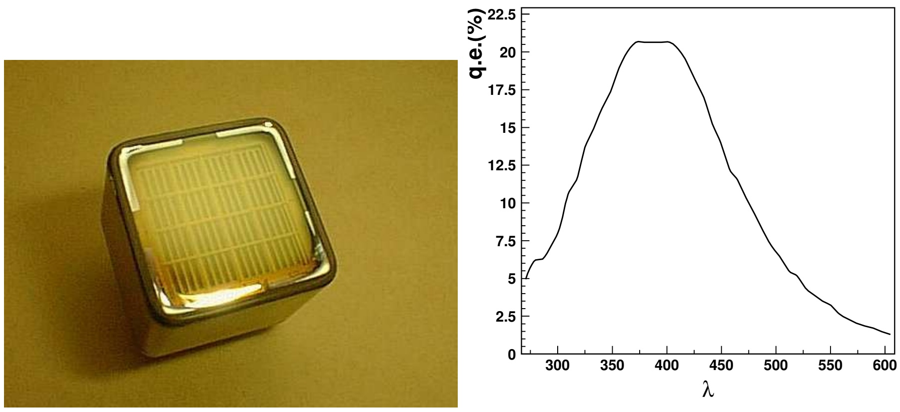

Figure 3.5: A Hamamatsu PMT R7600-M16-00 (left) and its quantum efficiency versus photon wavelength (right).

The Hamamatsu R7600-00-M16 fulfills these requirements[4]. It is a metal channel dynode PMT with a bialkali cathode and gives a maximum wave-

[4]An exhaustive study of the performance of this PMT can be found in [48].

length response at $\sim$400 nm. Figures 3.5 shows a photograph of this phototube and the plot of quantum efficiency versus photon wavelength.

The cathode area is 18.1$\times$18.1 mm^2, and is divided in 4×4 pixels. It has fast response, with an anode pulse rise time of 0.83 ns, and has low anode dark current (of about 1 nA). The photocathode material is deposited on a borosilicate glass window which allows a good photon transmission to approximately 300 nm.

The charge multiplication is obtained through a 12-dynode system and the gain is about 10^6 at 800 volts. The s.p.e. resolution is $\simeq$ 50% and the response is expected to be linear up to $\simeq$80 p.e.

Despite the good PMT behavior under magnetic fields, the AMS high residual field at the PMT plane ($\sim$ 300 G) forces the inclusion of a magnetic shielding.

Light is collected by means of plastic light guides positioned on top of the PMT and connected to the PMT window with a flexible optical pad of 0.5 mm thickness. Each guide has 16 individual guide pipes, one for each PMT pixel.

3.5.3 Expected performance

The momentum threshold of the RICH is given by $p_{th} = m/\sqrt{n^2-1}$, which results to be $\sim$ 2.9 GeV/c for protons for an aerogel of refractive index $n = 1.05$ and 1.1 GeV/c for NaF. The reconstruction efficiency for the sample above threshold is expected to be $\geq$ 70% for protons and $\geq$ 80% for heavier nuclei. The β measurement will be performed with a resolution of $\sim$ 0.1% for protons and improving with the number of collected photoelectrons until the saturation limit ($\sim$ 0.01%) is reached. For what concerns the charge measurement, it will be possible to identify nuclei up to Iron with a charge confusion of $\sim$ 10%. In next chapter the charge reconstruction capabilities will be illustrated in detail.

The expected performances of AMS after 3 years on the ISS have been already illustrated in section 2.3.7. The contribution of the RICH to these measurements is of fundamental importance, especially for isotope separation. In figure 3.6 the expectations for different signals are shown: the ^{3}He/^{4}He ratio versus kinetic energy per nucleon (left plot), and the Be^{10}/Be^9 ratio [15].

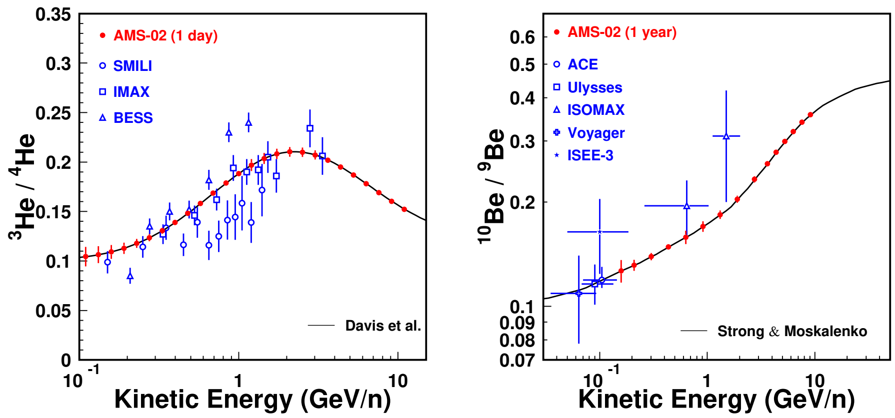

Figure 3.6: Expected performance of AMS-02 on the ISS. Left: ^{3}He/^{4}He ratio versus kinetic energy per nucleon. Right: ^{10}Be/^{9}Be ratio. The data are simulated with a statistics corresponding to 1 day and 1 year of data taking respectively.

Chapter 4

Charge reconstruction with the AMS RICH

In this chapter we will present an algorithm for charge reconstruction. The basic idea of the algorithm is to calculate the number of expected photoelectrons for a particle, assuming it had charge one, and to compare it with the number of photoelectrons actually measured for the event.

In this chapter the assumptions at the basis of this method will be explained (section 4.1.2), and its structure will be described (section 4.2), finally the results obtained with the RICH simulation will be shown (section 4.3).

4.1 Introduction to the RICH software

The task of the RICH reconstruction software is to compute the velocity and the charge for each charged particle from the detected Čerenkov light. The input track parameters are assumed to be provided by the AMS tracker.

The RICH reconstruction code has two different packages: first, the particle velocity is reconstructed from the ring pattern on the photodetection plane and then the charge is computed from the associated signal.

4.1.1 Velocity reconstruction

The algorithm for β reconstruction has already been written and implemented in the AMS software [17]. Here it will be briefly described to introduce the charge reconstruction in the context of the RICH software.

The signature of a particle above the Čerenkov threshold consists of a set of hits[1]; each one characterized by a position (x, y) on the detection plane, and a signal in terms of photoelectrons.

The purpose of the algorithm is to compute a value of β for each detected hit (β_{hit}) and to identify those which are due to Čerenkov photons and then determine the velocity of the incident particle.

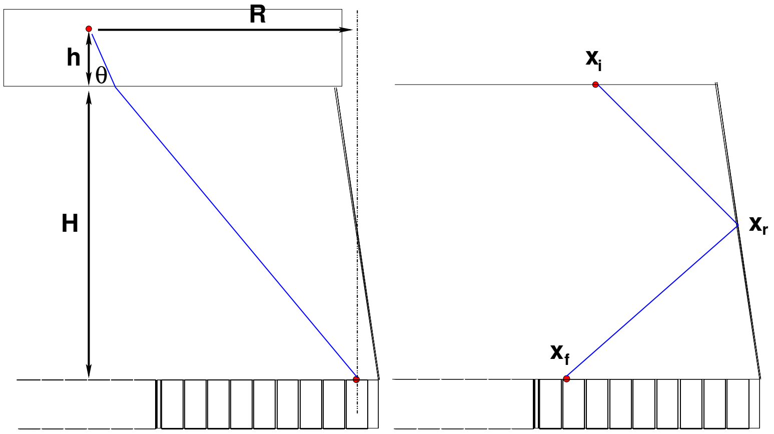

Figure 4.1: Display of a photon trajectory directly detected (left) and detected after one reflection onto the mirror (right).

The algorithm is structured in three steps:

1. For each hit the value of β_{hit} is computed under the assumption of being direct (as shown in left panel of figure 4.1) and of being reflected onto the mirror (rigth panel of figure 4.1). This latter case gives two possible solutions due to the geometry of the problem. In total, one has at most 3 possible values of β_{hit} for each hit.

2. The reconstructed values of β_{hit} are grouped in clusters and a weight is associated to each of them depending on its narrowness and on the number of elements.

3. The cluster with the highest weight is identified with the ring image, and the β of the event is obtained computing the mean of the β_{hit} of the cluster weighted by their corresponding number of photoelectrons.

[1] a hit is defined as a signal above the detection threshold.

4.1.2 Charge reconstruction

As explained in the previous chapter (section 3.1), the differential number of photons produced by the transit of a charged particle through a radiator material is given by:

$$\frac{d^2N}{dxdE} = \alpha Z^2 \left(1 - \frac{1}{(n\beta)^2}\right) \tag{4.1}$$

and therefore proportional to the square of the charge.

Once the velocity has been determined, one can calculate the number of expected photoelectrons in the ring assuming the particle had charge 1 (we will call this quantity N_{exp}) simply integrating equation 4.1.

This algorithm intends separate particles of different charge counting the number of photoelectrons, so the limitation in charge determination is expected to come from statistical fluctuations in the number of detected Čerenkov photons. This assertion can be quantitatively expressed with the following argument: for a particle of charge Z the number of observed photoelectrons (N_{seen}) is a quantity assumed to be distributed following a Poisson, with mean value Z^2N_{exp}. In the following it will be convenient to express N_{seen} as:

$$N_{seen} = Z^2N_{exp} \pm kZ\sqrt{N_{exp}} \tag{4.2}$$

An estimator for the charge can be constructed by minimizing the square of the residue:

$$E(Z) = \frac{(N_{seen} - Z^2N_{exp})^2}{Z^2N_{exp}} \tag{4.3}$$

Since at the minimum $E(Z) < E(Z \pm 1)$; after substituting the expression 4.2 in 4.3 it is straightforward to obtain that:

$$k^2 < N_{exp} \tag{4.4}$$

From this result it is obvious that the charge confusion:

1. is independent of the charge of the particle;
2. is directly related to the number of expected photoelectrons for a kinematically equivalent $Z = 1$ particle (N_{exp}).

4.2 The charge reconstruction algorithm

4.2.1 Selection of hits

The quantity N_{seen} is experimentally estimated for each event adding up the signals associated to the hits which belong to the ring image. At first approximation, we will consider those hits which have been used in the β reconstruction. Only in case of high Z (> 6) particles the selection criterion of good hits must be optimized in order to avoid the possibility of counting hits of very high charge, due to the mother particle. In this case, the signal of the associated hits must be lower than a given value when their reconstructed β under the assumption of being direct is near the threshold.

After selecting the set of hits, the total number of photoelectrons is computed in terms of the photomultiplier single photoelectron response:

$$N_{seen} = \sum_{1}^{N_{used}} N_{pe} \tag{4.5}$$

where N_{used} is the number of used hits, N_{pe} is the signal is terms of photoelectrons of a single hits: $N_{pe} = \frac{Q}{G}$ where G is the gain of the photomultiplier, Q is the signal of the hit.

4.2.2 The calculation of N_{exp}

The calculation of N_{exp} is made individually for each event integrating by a numerical method the differential equation:

$$\frac{d^2N}{dxd\lambda} = 2\pi\alpha\frac{q(\lambda)}{\lambda^2}\sin^2\theta_c(n,\beta) \tag{4.6}$$

where q is the quantum efficiency of the photocathode. The variable x has to be integrated along the particle path in the radiator and λ over the range of the photocathode sensitivity (from about 260 to 600 nm). The algorithm takes as input:

- the reconstructed β of the particle;
- the particle track parameters on top of the radiator.

Starting from the impact point of the particle on top of the radiator, a number of rays (NSTP) on a conical surface around the particle trajectory are propagated through the RICH to the detection plane. This procedure is repeated NSTL times along the particle path inside the radiator.

The numerical integral can be written as:

$$N_{exp} = \int d\lambda\, d\phi\, dx\, \alpha \frac{q(\lambda)}{\lambda^2} \sin^2\theta_c(n,\beta)\, eff(\vec{r},\vec{u})\, f(l_r, l_f, l_g) \tag{4.7}$$
$$\sim \alpha \sum_{i=1}^{NL} \Delta\lambda_i \frac{q(\lambda_i)}{\lambda_i^2} \sin^2\theta_c(n,\beta) \Delta x \sum_{i=1}^{NSTL} \Delta\phi \sum_{j=1}^{NSTP} eff(\vec{r}_i,\vec{u}_j)\, f(\vec{r}_i,\vec{u}_j)$$

where $eff(\vec{r}_i,\vec{u}_j)$ stands for the ray detection efficiency, $\vec{r}_i$ and $\vec{u}_j$ are the ray origin position and direction respectively and f is a term of photon loss explained later.

For each integration step the ray tracing computes a number $(eff(\vec{r}_i,\vec{u}_j))$ which expresses the geometrical efficiency for that ray.

In order to speed up the procedure, the λ dependent term has been factorised from the geometrical efficiency, which has no significant dependence[2] on it.

All the factors which could affect photon propagation from the radiator to the photocathode have been included in the calculation of the ray efficiency:

- the active aerea of the detector, rejecting rays which go to the ECAL hole or to the gap between light guides;
- the reflection on the RICH conical mirror, considered as a perfectly smooth surface with reflectivity 0.85;
- the light guide efficiency, computed with a simulation using the GEANT package. The efficiency is tabulated as function of the direction of the ray (θ, ϕ) and the light guide pipe type;
- the separation between radiator tiles.

The same ray tracing function also returns the path length crossed by the ray inside the radiator (l_r), inside the support foil (l_f) and in the light guide (l_g). On the basis of these values the factor f, consisting in the photon losses due to absorption inside these materials and to the Rayleigh scattering, is computed as:

[2] The effect of the radiator chromatic dispersion, n(λ), can be safely neglected without compromising the global precision of the algorithm.

$$f(l_r, l_f, l_g) = e^{-l_r C/\lambda^4} e^{-l_r/L_{absr}} e^{-l_f/L_{absf}} e^{-l_g/L_{absg}} \tag{4.8}$$

where L_{absr}, L_{absf}, L_{absg} are the absorption lengths in the radiator, foil and light guide materials respectively. Although f depends on λ, the integration is computed only once at the first call of the reconstruction and then the values of f for different values of l_r, l_f and l_g are tabulated.

The total number of rays traced is the product of the number of integration steps along the track path length inside the radiator times the number of steps around the trajectory.

4.3 Results

4.3.1 Flight setup

The algorithm has been tested with the RICH simulation, based on the GEANT simulation package. As input to the reconstruction, the track has been taken from the generator and the β from the output of the reconstruction.

The setup considered is the following:

- 680 photomultipliers
- light guides of 3.4 cm side
- radiator aerogel, refraction index 1.05
- pitch between photomultipliers of 3.7 cm
- 3 cm radiator thickness

Here we show results for four different samples of particles: protons, helium, carbon and aluminum. For each particle species two different samples have been simulated, one with an uniform beta spectrum between the Čerenkov threshold and $\beta \sim 1$, and another with the fixed value of $\beta = 0.9999$.

The event selection requires a loose cut on the reconstructed beta ($|\beta_{recon}/\beta_{gen} - 1| < 0.2\%$). This requirement, which is only nedeed to check the charge algorithm performance with high charge samples, is kept for consistency for low charge samples. The percentages of each sample that fulfil this requirement are shown in table 4.1. All the results shown in the following will refer to the sample above defined.

	$\beta \sim 1$	uniform β
p	86%	91%
He	97%	97%
C	97%	97%
Al	97%	95%

Table 4.1: Fractions of events with reconstructed β that fulfil the condition of $\Delta\beta < 0.2\%$.

4.3.2 Distribution of the number of expected photoelectrons for a Z=1 particle

In figure 4.2 the distribution of expected photoelectrons is displayed for the sample of $\beta \simeq 1$, at different levels in the RICH from the generation inside the radiator down to the detection at the photocathode. The photomultiplier quantum efficiency is already applied at the generation level.

Figure 4.2(a) is the distribution of photons generated inside the radiator, obtained simply integrating the differential equation of Čerenkov spectrum (eq. 4.6). The plot shows a very sharp peak at ~ 40 photons. The spread of the distribution depends on the different path lengths in the radiator.

At the second level we consider the photons exiting the bottom surface of the radiator (figure 4.2(b)). Rayleigh scattering shifts the peak down to ~ 18 photons and, in addition, photon losses due to the opaque separation between tiles of radiator cause the tail to lower values.

After propagating in the expansion volume, photons reach the upper surface of the light guides (figure 4.2(c)). The peak of the distribution for fully contained events is further shifted to ~ 13 photons due to different sources of inefficiency, mainly photon losses in the gaps between guides and in the corners between ligth guide grids and mirror (the effective area efficiency is $eff_A \simeq 0.78$). Mirror reflectivity also contributes (with a factor $\simeq 0.93$) given that on average half of the photons forming the ring of fully contained events have been reflected. A migration from the peak to lower values is observed, due to photons lost in the E-CAL hole.

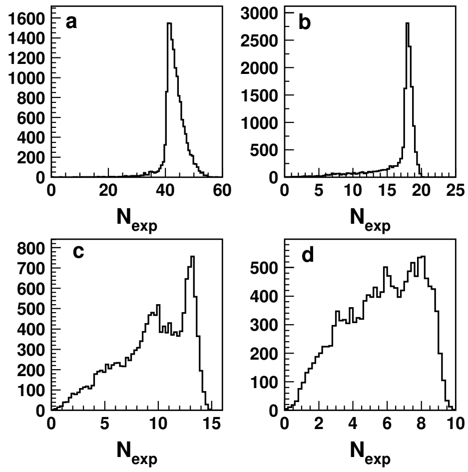

Figure 4.2: Distribution of expected photoelectrons at four different levels: at the generation inside aerogel (a), exiting from radiator (b), arriving at the base on light guide top surface (c), detected at the photocathode (d). The photomultiplier quantum efficiency is already applied at the generation level.

Finally, we consider the photons reaching the photocathode, namely the photoelectrons (figure 4.2(d)): all the effects mentioned in section 4.2.2 are included. The application of light guide efficiency shifts the maximum of the distribution from 13 to ~ 8 photons. In addition to this, the inhomogeneity of light guide efficiency in position and direction causes a further smearing of the distribution.

The profile histograms of the reconstructed number of photoelectrons in the ring (N_{seen}) versus N_{exp} are shown in figure 4.3 for protons, helium and carbon. The continuous lines are the theoretical curves, with slope Z^2. There is good agreement between simulation and reconstruction. A more sensitive quantity to test the precision of the algorithm is the residue (plotted in figure 4.4 for the four samples studied):

$$R_Z(N_{seen}, N_{exp}) = \frac{N_{seen} - Z^2 N_{exp}}{Z\sqrt{N_{exp}}} \tag{4.9}$$

which, by construction, should be centered at zero and have standard deviation close to $\sqrt{1 + (\sigma/G)^2} = \sqrt{5/4}$ for a 50% single photoelectron (s.p.e.)

atomic number	mean value	width
1	0.080	1.092 (RMS)
2	0.028	1.105
6	-0.014	1.179
13	-0.059	1.319

Table 4.2: Parameters resulting of a Gaussian fit applied to the distributions in figure 4.4: mean value and width. For protons the Gaussian approximation is not valid, for the very low number of detected photons; the values displayed in the table are mean value and RMS of the distribution.

resolution, as included in the simulation.

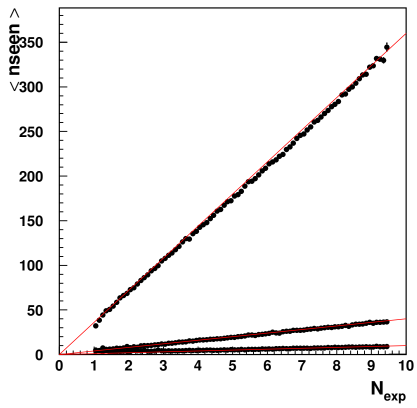

Figure 4.3: N_{seen} versus N_{exp} for 3 different samples. The slopes of the curves are in good agreement with the theoretical values (i.e. Z^2)

A lack of precision on the computation of N_{exp} will cause a broadening of this distribution which is expected to be more important for high Z, as can be noticed in table 4.2.

4.3.3 Reconstructed charge

The distribution of $Z = \sqrt{N_{seen}/N_{exp}}$ is shown in figure 4.5. After a cut of $N_{exp} > 3$ (shadowed area in the histograms) the distributions are narrower

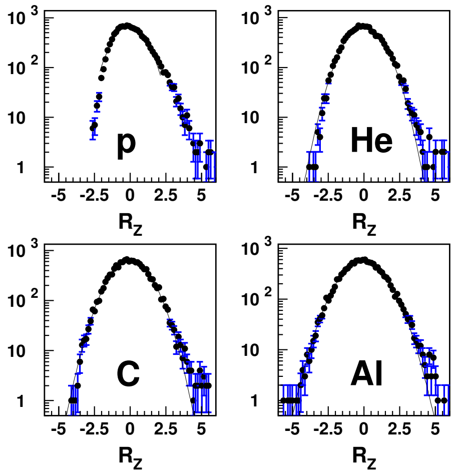

Figure 4.4: Residue distributions: $R_Z(N_{seen}, N_{exp}) = \frac{N_{seen} - Z^2 N_{exp}}{Z\sqrt{N_{exp}}}$

and the tails are suppressed. The σ of the Gaussian fits vary from 0.22 (protons) to 0.28 (Aluminum). The reconstructed integer charge can be estimated applying on event by event basis a maximum likelihood method. This method consists in finding the number $Z \in \mathcal{N}$ that maximizes the probability of measuring $N = N_{seen}$ photoelectrons if the mean of the distribution is $\mu = Z^2 N_{exp}$:

$$P_\mu(N) = \frac{\mu^N}{N!} e^{-\mu} \tag{4.10}$$

For each event we substitute in equation 4.10 the current values of N_{exp} and N_{seen}, and obtain the value for the most probable charge.

The results are shown in figure 4.6.

4.3.4 Charge confusion

The charge confusion is defined as the fraction of events reconstructed with a wrong charge. In figure 4.7 the differential charge confusion versus N_{exp} is shown for the four particle species. Full marks are relative to the sample of $\beta \simeq 1$ and empty marks to the sample of uniform β.

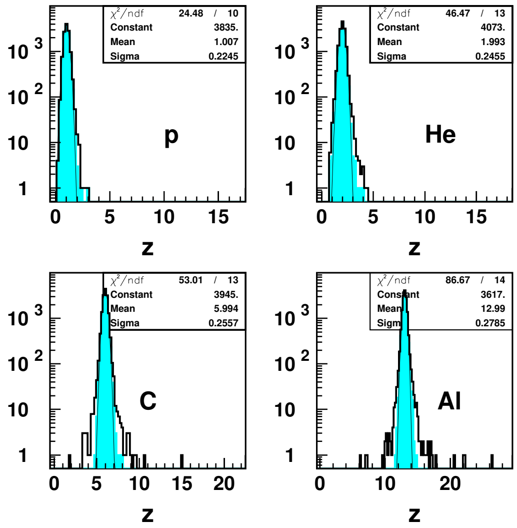

Figure 4.5: Continuous distribution of the charge. White histograms: all the reconstructed events, shadowed areas: events with $N_{exp} > 3$.

As expected, the charge confusion only depends on the number of expected photoelectrons and decreases with it. Particles with a high number of expected photoelectrons generate a light cone through a zone of higher acceptance of the RICH, allowing a better charge identification.

The obtained values of charge confusion are compared with the theoretical expectation under the assumption of different uncertainties of N_{exp}.

The results of the comparison are presented in figure 4.8 and show that the uncertainty in the computation of N_{exp} is at level of 2%.

In figure 4.9 the integral charge confusion versus the number of expected photoelectrons is shown for samples of beta$\simeq$1. In table 4.3 the values corresponding to a cut $N_{exp} > 6$ are included. The efficiency of this cut is about 50% with respect to the initial selected sample as described in section 4.3.1.

4.3.5 Sensitivity to track parameters

As pointed out in section 4.2.2 the charge reconstruction needs as input the track parameters of the mother particle. A study of the sensitivity of

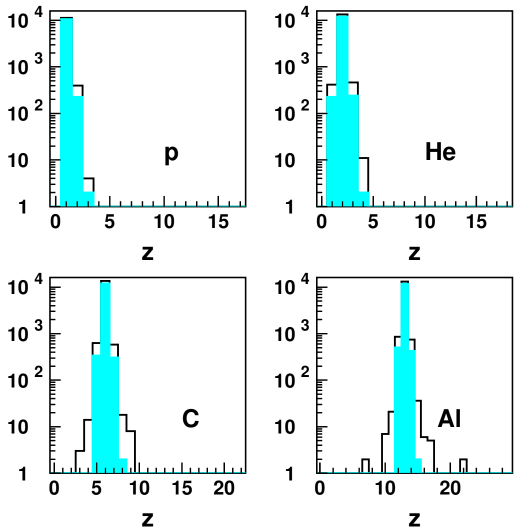

Figure 4.6: Reconstructed charge, shadowed area is relative to events with $N_{exp} > 3$.

atomic number	integral charge confusion
1	1%
2	1.8%
6	2.7%
13	4%

Table 4.3: Integral charge confusion for the cut $N_{exp} > N_{min} = 6$.

the reconstruction to track position and direction has been made simulating a Gaussian smearing of the track parameters taken from the generator. In figure 4.10 the quantity in the x axis is the uncertainty on the particle position on top of radiator and in the y axis the integral charge confusion. For protons and helium the effect is negligible, whereas for high Z elements, for example $Z = 13$, the charge confusion doubles for a track indetermination of about 0.1 cm. Since the expected precision on the AMS track extrapolation at the RICH radiator is expected to be $\simeq 0.02$ cm the effect of the position uncertainty on the N_{exp} computation is expected to be negligible.

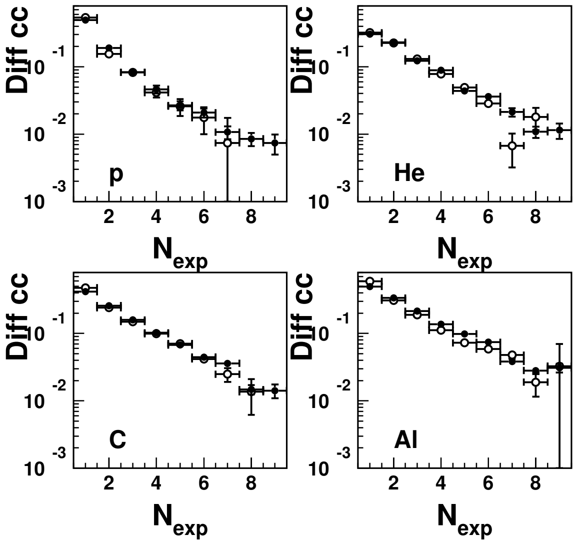

Figure 4.7: Differential charge confusion. Full marks are relative to the spectra of beta $\simeq$1 and empty marks to the spectra of uniform beta.

4.3.6 Reconstruction time

The Z reconstruction time, t_Z, only depends on the number of intervals of integration, NSTEPS (as explained in section 4.2.2):

$$t_Z \propto NSTEPS = NSTL \times NSTP \tag{4.11}$$

t_Z does not depend on the features of the event to reconstruct, like number of hits or charge. However, for high Z particles the number NSTEPS must be increased in order to keep the precision of the computation within a 2%. In figure 4.11 the reconstruction time has been compared with that of the RICH β reconstruction. The β reconstruction time (see [17]) has a strong dependence with the number of hits ($t_\beta \propto N_{hits}^2$). As a consequence, the charge reconstruction is 30 times slower for protons, and is only $\sim$2 times slower for Aluminum.

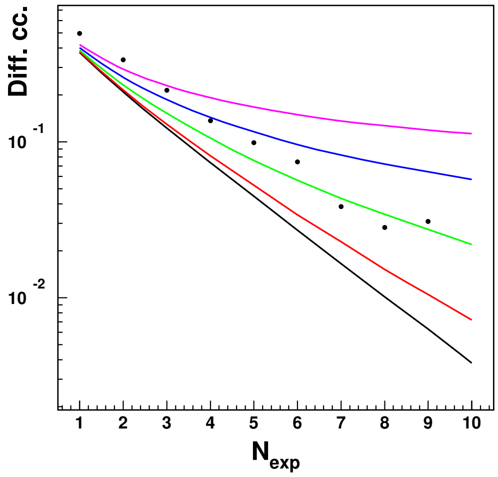

Figure 4.8: Differential charge confusion: full marks are values from a simulated sample of Al, continuous lines are theoretical prediction with different values of uncertainty on N_{exp}: black curve 0%, red curve 1%, green curve 2%, blue curve 3%, purple curve 4%.

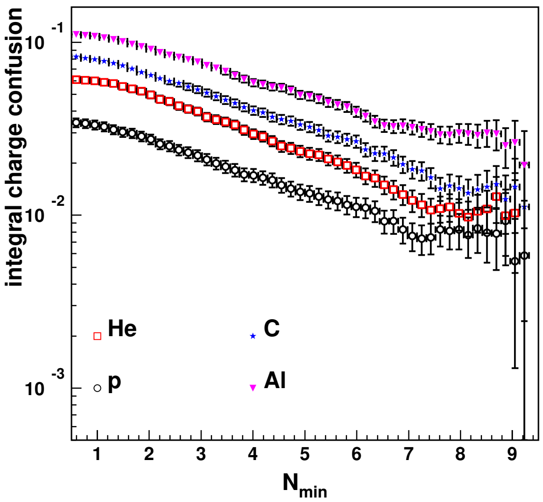

Figure 4.9: Integral charge confusion versus N_{exp} for $\beta \sim 1$ samples.

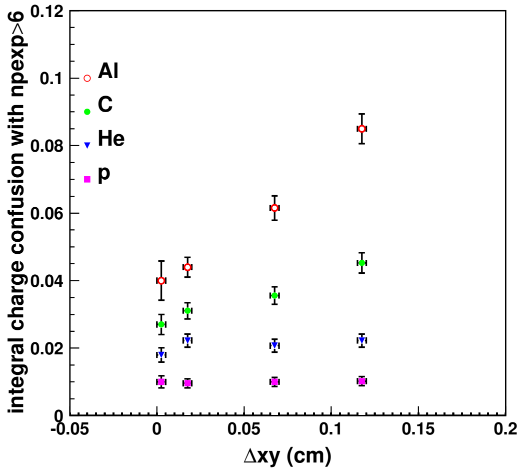

Figure 4.10: Integral charge confusion versus N_{exp} for $\beta \simeq 1$ samples versus track position uncertainty.

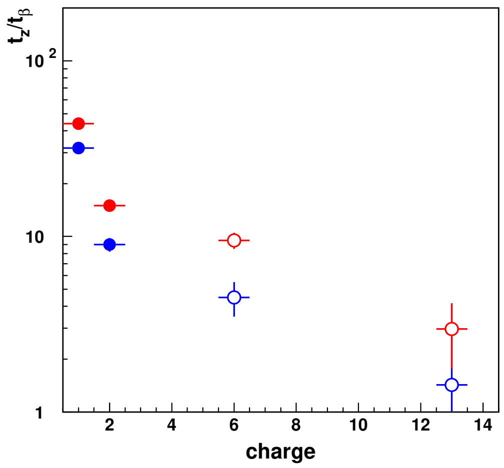

Figure 4.11: t_Z/t_β. Empty marks: NSTEPS=6400, full marks: NSTEPS=1050. Red marks: uniform β, blue marks: $\beta \simeq 1$

Chapter 5

Results with the RICH prototype

5.1 Introduction

The feasibility of the RICH detector has been checked with a prototype consisting essentially of one block of radiator and a detection plane instrumented with 96 photomultipliers (PMTs), representing $\sim 14\%$ of the total number of channels. The prototype has been used to test most of the hardware of the final RICH detector and its capabilities for velocity and charge reconstruction.

The RICH prototype has been operating in two different configurations. First, from March to August 2002, at the ISN (Grenoble) for cosmic muons data taking. Then, from 14 to 19 October 2002, at the CERN SPS for a test beam with ions, where the AMS tracker and TOF prototype were also present. In the following I will refer to the first configuration as CM (=Cosmic Muons), and to the latter as TB (=Test Beam).

In this chapter a short description of the prototype will be given (see [18] for details) and some preliminary results on charge analysis will be shown.

5.2 The experimental setup

The RICH prototype consists of a radiator block and an array of 96 Hamamatsu multianode PMT[1] R7600-00-M16 arranged in a rectangular matrix, all enclosed in a ligth tight box. On top of each PMT a light collection system formed by 16 light guide pipes provides light transmission to the PMT cathode window. The PMTs and front end electronics are the same as for the final RICH design. Several types of silica aerogel (Agl) with refractive index (n) in the range $1.03 < n < 1.05$ produced by the Catalysis Institute of Novosibirsk [32] and by Matsushita Electric Works [28] have been tested, in order to choose the most suitable one for the RICH detector.

The top view of the light guides forming the detection plane is shown in figure 5.1. The pitch between two consecutive guides is 3.1 cm, resulting in a $\simeq 100\%$ active area over the light guide plane.

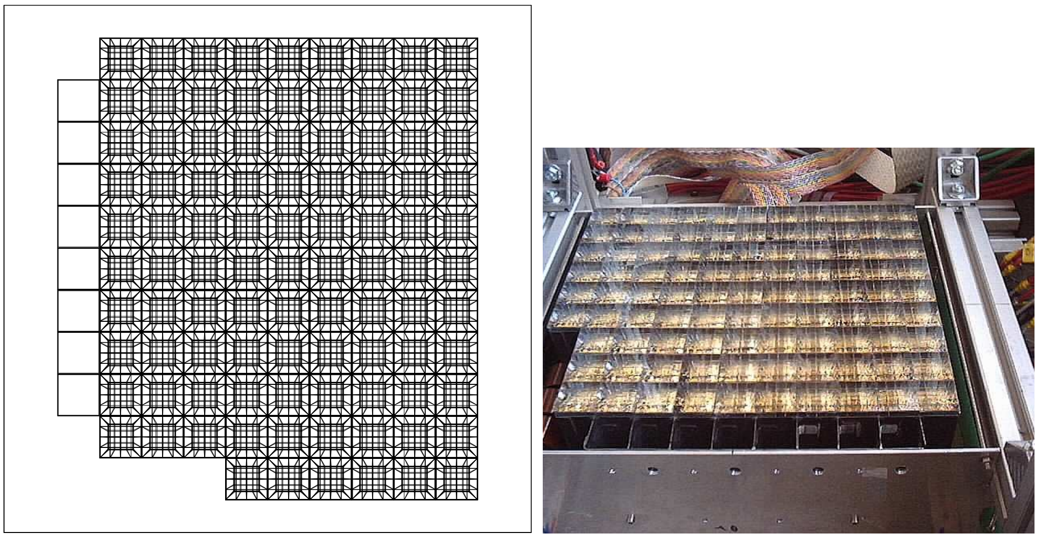

Figure 5.1: Upper view of the light guide matrix of the prototype: in the left panel the layout of the simulation, in the right panel a photograph.

The setup was completed with two scintillator paddles, which provided the trigger by coincidence and an additional particle charge determination, and with multiwire proportional chambers (MWPC) to determine the particle track.

[1] 16 pixels in a 4x4 matrix

Track determination

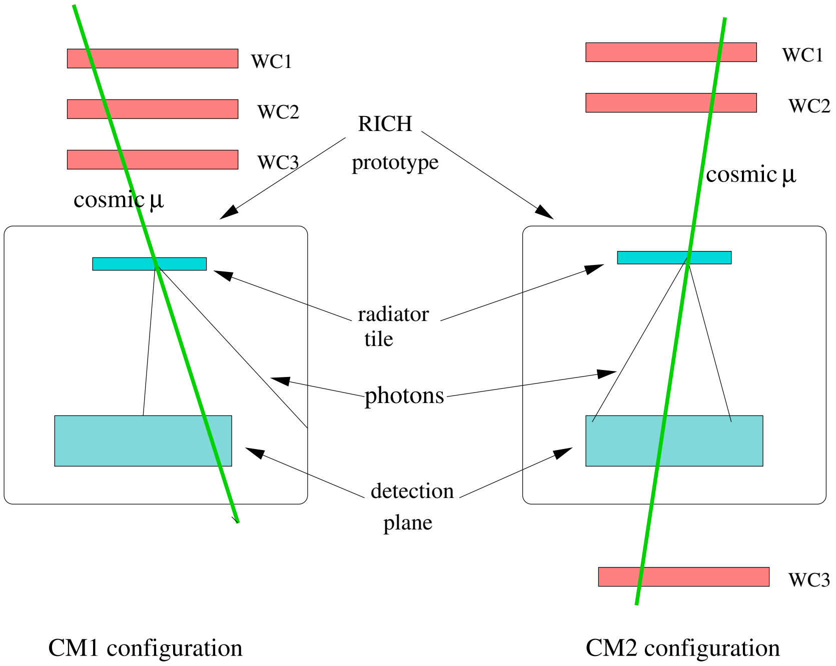

Figure 5.2: Schematic view of the setup for the two CM setups.

In the CM configuration the track determination was provided by 3 planes of MWPC. In the first period of data taking the 3 planes of the MWPC were placed above the prototype (figure 5.2 left). Later, one of the plane was moved below it to improve the track determination (figure 5.2 right).

In the TB configuration, shown in figure 5.3, the track determination was provided by a beam chamber constituted by a MWPC in the vertical (y) direction and by a Si microstrips chamber in the horizontal (x) direction. Assuming that the track is perpendicular to the radiator plane, a single measurement along the particle trajectory is sufficient to determine the track. The precision of the track determination in the different configurations is shown in table 5.1.

In the simulation the track detector resolution is included as a smearing in the track position, with the adecuate spread.

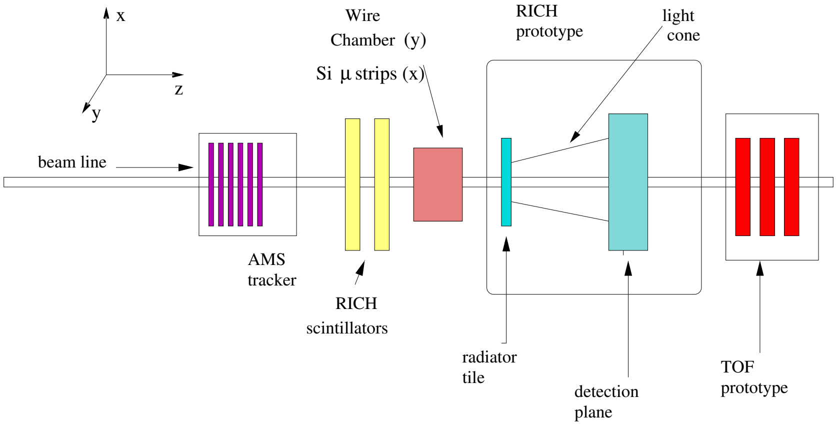

Figure 5.3: Schematic view of the setup for the test beam at beam line H8 of CERN-SPS. From the left: the tracker prototype, the scintillator paddles, the beam chamber, the RICH prototype and the TOF prototype are shown. The distances are not at real scale.

detector	coordinate	estimated resolution (cm)	setup
Si microstrips	x	0.021	TB
MWPC	y	0.099	
MWPC	x and y	0.28	CM1
MWPC	x and y	0.08	CM2

Table 5.1: Resolution on track measurement with different track detectors [18]

The scintillator counters

In both prototype configurations, the trigger was provided by the coincidence of the signals in two scintillator paddles. In the TB setup these counters had the additional purpose of providing an independent particle charge determination.

The correlation between the scintillators anode and dynode signals and the reconstructed RICH charge has been studied. The lack of linearity in the scintillator response and their poor resolution made quite difficult to construct a reliable charge calibration for them. An estimation of the RICH charge confusion has been obtained using TOF prototype data for an external charge determination.

The radiators

A good radiator must fulfill different requirements. In order to provide a good β resolution, it must have a low refractive index (see section 3.3.1). At the same time, the photon yield has to be high enough to keep a good reconstruction efficiency. Moreover, as we saw in section 4.3.4, the charge confusion improves with the number of expected photoelectrons.

One of the objectives of the prototype was to test the performances of different radiators and for this purpose several radiators have been used during data taking. In table 5.2 all the radiators are listed and for each one the manufacturer, the refractive index and the radiator tickness are speficied.

manufacturer	refractive index	thickness
Matsushita	1.03	2 cm
Matsushita	1.05	2 cm
Novosibirsk	1.03	3 cm
Novosibirsk	1.04	3 cm

Table 5.2: Optical properties of two different kinds of aerogel both produced by Matsushita.

In addition to the aerogel radiators listed in table 5.2, also a sample of NaF has been used, with refractive index 1.33 and 0.5 cm thickness.

With the CM setup only Matsushita aerogels and sodium fluoride have been tested, the results are shown in section 5.3.

In the TB configuration all the samples have been tested, and from a preliminary analysis it results that regarding charge reconstruction the best performances have been obtained with the Novosibirsk 1.03 and with Matsushita 1.05. Some results relative to the Novosibirsk aerogel of index 1.03 are illustrated in section 5.3.2.

5.3 Results

5.3.1 Results with cosmic muons

The samples analysed have been selected with the following requirements:

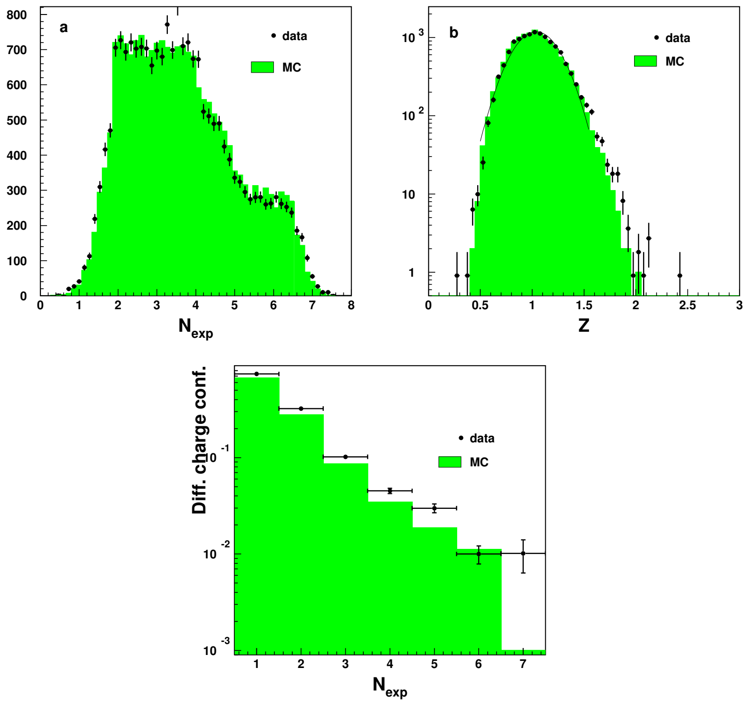

Figure 5.4: Plots relative to Run 21 of prototype with Matsushita aerogel of refractive index 1.03 of 3 cm thickness. a) N_{exp} distribution; b) charge distribution; c) differential charge confusion versus N_{exp}.

1. good quality for the reconstructed track.

2. good quality for the reconstructed β (β_{rec}). This is achieved with these conditions: first, $N_{used} > 2$. Then, the β_{rec} is consistent with the β calculated excluding the PMT hit by the particle.

3. $N_{exp} > 3$ for all the runs but for NaF, where this cut was relaxed to $N_{exp} > 2$ because of the low photon yield of the radiator.

The charge distribution for the sample of Matsushita aerogel of refractive index 1.03 is shown in figure 5.4(b) for the Monte Carlo simulation (the shadowed aerea) and data (full marks). The charge resolution is 0.21 charge units[2] for data and 0.20 for the Monte Carlo. In 5.4(a) the distribution of

[2]in the following all the values of charge resolution are expressed in charge units

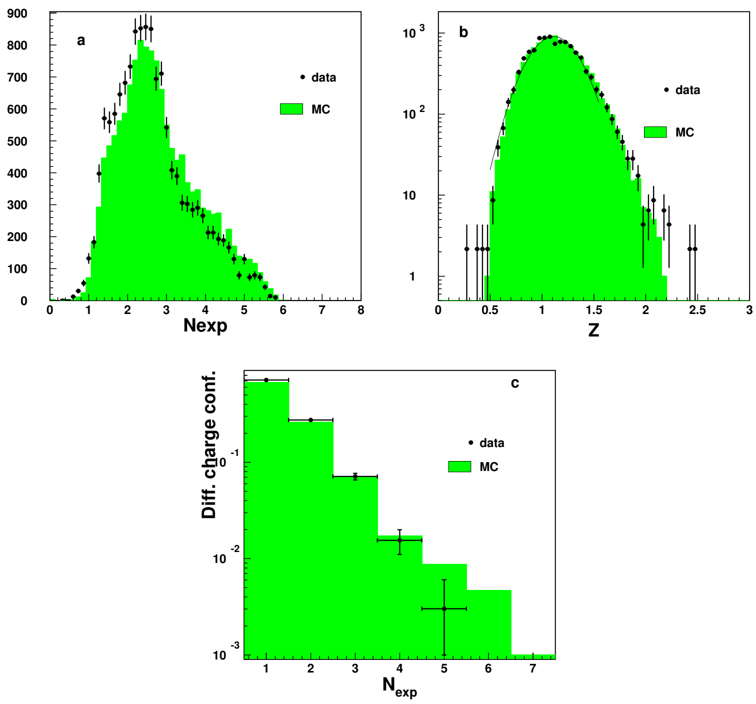

Figure 5.5: Plots relative to run 26, with a radiator Matsushita aerogel of refractive index 1.05 of 2 cm thickness. a) number of expected photoelectrons, b) charge distribution, c) differential charge confusion versus number of expected photoelectrons.

expected photoelectrons is shown.

In figure 5.5 the same plots for a run with Matsushita aerogel of index 1.05 and 2 cm thickness. The estimated charge resolution is 0.22 in both data and Monte Carlo simulation. Finally in figure 5.6 the results for a run with a radiator tile of sodium fluoride of 0.5 cm thickness. In this last case the resolution is worse, (0.29 for data and 0.26 for MC) due to the low photon yield.

We notice that for all the runs the differential charge confusion decreases with the N_{exp}, as expected from the simulation.

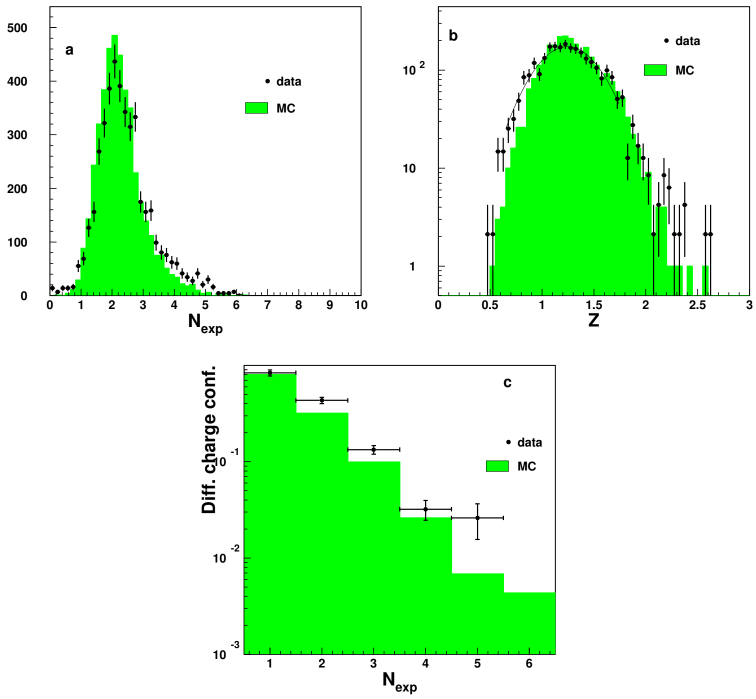

Figure 5.6: Same plots of figure 5.5 a,b,c, for run 29 of NaF, of 0.5 cm thickness.

5.3.2 Results with test beam

The prototype was placed in the experimental area of H8 of CERN-SPS, together with the prototype of the tracker and that of the TOF, as shown in figure 5.3.

The beam

The beam consisted in ions of Pb of 20 GeV/c/nucleon interacting with a target of Beryllium. Setting the beam conditions, beams with different values of the mass to charge ratio (A/Z) have been selected:

- A/Z=1: beam of protons, of different momenta.
- A/Z=3/2: beam of ^{3}He.
- A/Z=2: beam of most of the stable isotopes.

The momentum of the beam was given with a precision of 2% and the beam angular divergence was ≤ 3 mrad.

In this work we will show results relative to the runs number 310, 312 and 313 taken with the radiator Novosibirsk with refractive index 1.03 and 3 cm thickness.

These results refer to samples selected following these requirements:

1. the track has been well reconstructed by beam chamber, and there is good matching between the track extrapolation to the light guide plane and the position of the hit with highest charge. Moreover, the particle has passed through a zone of good acceptance of the radiatore tile. In some runs it has been noticed that particles impinging near the edge of the radiator tile give a lower photon yield, because of photon losses at the radiator edge. The efficiency of these geometrical cuts is $\sim 31\%$ for the run of protons, $\sim 36\%$ for $A/Z = 3/2$ and $\sim 50\%$ for $A/Z = 2$. The values of efficiency differ due to the different beam conditions.

2. Events with a number of expected photoelectrons significantly lower that the mean value of the distribution are discarded. This means: $N_{exp} > 6.5$ for protons and $N_{exp} > 7$ for the other runs. Finally a cut of compatibility between the ring reconstructed by the charge algorithm and the position of the hits on the detection plane is applied. The efficiency of this cut is $\sim 87\%$.

Velocity measurement

The β measurement has been studied applying a Gaussian fit to the β distribution and the resolution results at level of 0.1% for protons and improving with the particle Z. The values obtained are shown in table 5.3.

aerogel sample	p $\sigma(\beta)/\beta \times 10^3$	He $\sigma(\beta)/\beta \times 10^3$
NV103	0.67±0.01	0.382±0.004

Table 5.3: Beta resolution for the Novosibirsk Agl from [18].

For high charge elements the beam chamber was not efficient and alternative β reconstruction algorithm has been used to reconstruct the data. This algorithm is able to reconstruct the particle track using a pattern recognition method and allowed to recover a significant part of the statistics of high Z ($Z > 17$) particles which saturate the beam chamber. In figure 5.7 black markers refer to the standard β reconstruction and red squares to the new method. In both cases the β resolution improves with increasing charge until the expected saturation limit is reached.

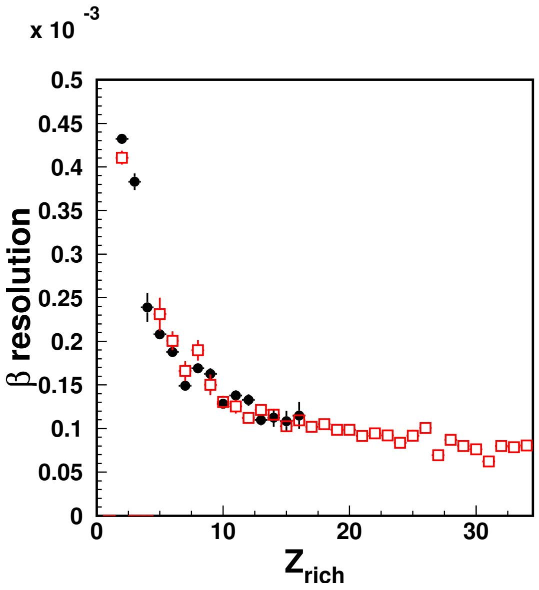

Figure 5.7: β resolution versus particle charge. Black and red markers refer to two different algorithms (see text).

Charge measurement

The results for a run of protons with 13 GV rigidity are shown in figure 5.8. The photon yield of this radiator was quite high, despite its low refractive index, as shown in figure 5.8, left. The distribution of expected photoelectrons has a very peaked shape, as expected for events fully contained in the detection plane.

The reconstructed charge has a Gaussian shape, due to the high mean number of photons (figure 5.8, right). The charge confusion is at level of 1% in both data and MC.

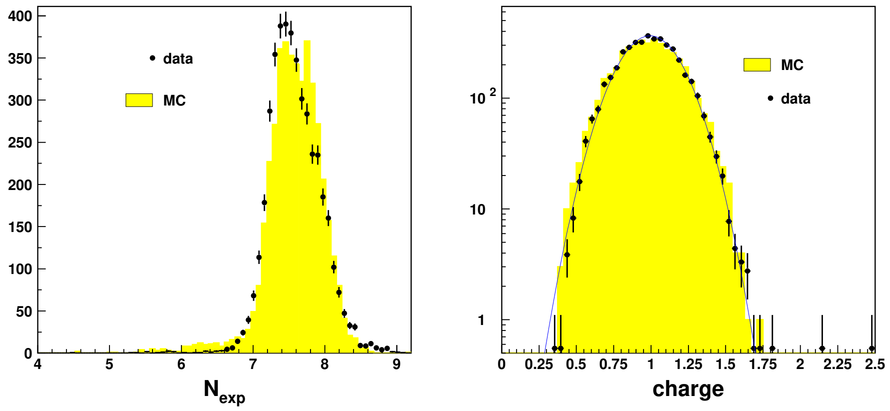

Figure 5.8: Left plot: Distribution of the expected photoelectrons for the run of protons; right plot: reconstructed charge. Data (black markers) and Monte Carlo (filled histogram).

The number of expected photoelectrons and the charge distribution for a run of ^{3}He of 30 GV rigidity are shown in figure 5.9. The distribution of N_{exp} has a main peak at ~ 8.3, corresponding to fully contained events, and a second one at ~ 7.7, which corresponds to rings formed near the border of the photodetection plane and thus not completely contained. In any case, the Monte Carlo simulation (filled histogram) reproduces the data (black markers) fairly well and the reconstructed charge has a Gaussian distribution with resolution 0.2 charge units.

The charge spectrum measured for a run of nuclei of 40 GV rigidity with ratio $A/Z = 2$ is shown in figure 5.10. The charge range extends from $Z = 2$ up to Z$\simeq$28 and the charge separation is good over all the spectrum.

A global fit consistent in a sum of Gaussian distributions has been applied to the charge spectrum and from the width of each Gaussian we have an estimation of the charge resolution, shown in figure 5.11. The continuous line shown in the plot is a theoretical limit computed on the basis of the observed number of expected photoelectrons for the run. It includes the photomultiplier s.p.e. response resolution and the uncertainty of the algorithm of charge reconstruction. At $Z > 20$ the very low statistics limits the quality of the fit.

An estimation of the RICH charge confusion has been computed using

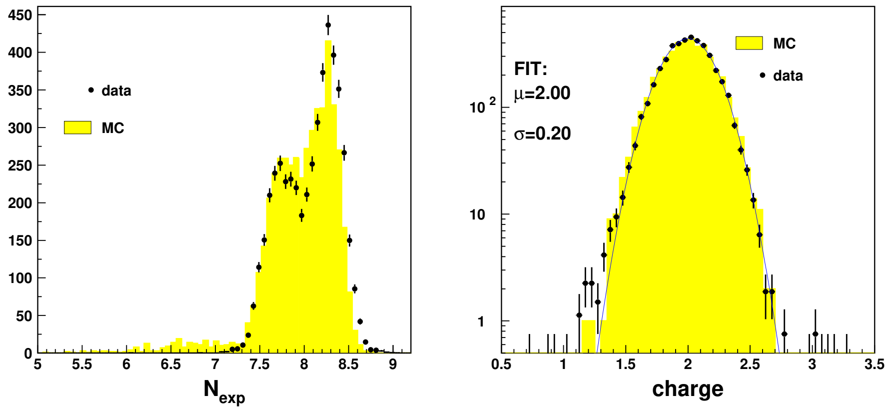

Figure 5.9: On the left number of expected photoelectrons and on the right charge distribution of He, data (black markers) and MC (filled histogram).

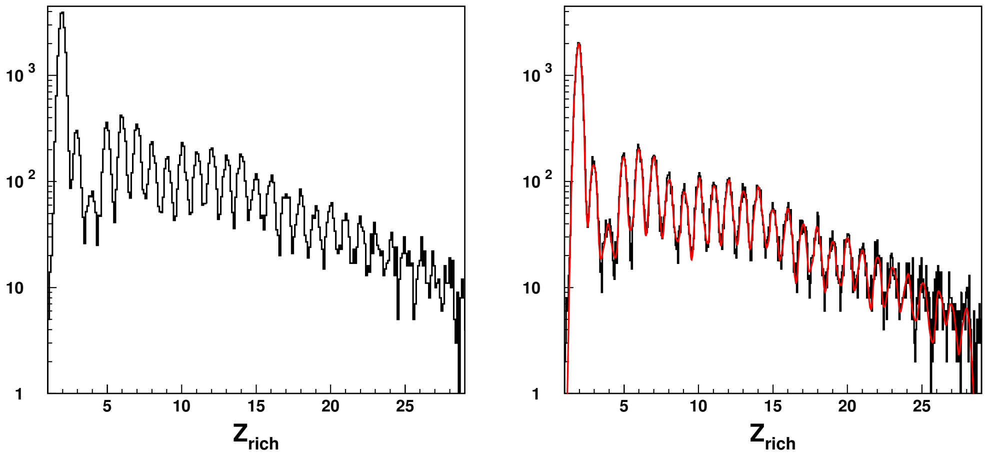

Figure 5.10: The charge spectrum of a run with $A/Z = 2$.

the TOF prototype data for an external charge determination. As shown in figure 5.3, a TOF prototype made up by three scintillators paddles was placed along the beamline after the RICH; a study of the correlation [21] of TOF charge measurement and the RICH reconstructed charge, shown in figure 5.12, has permitted to compute the RICH charge confusion up to $Z = 7$

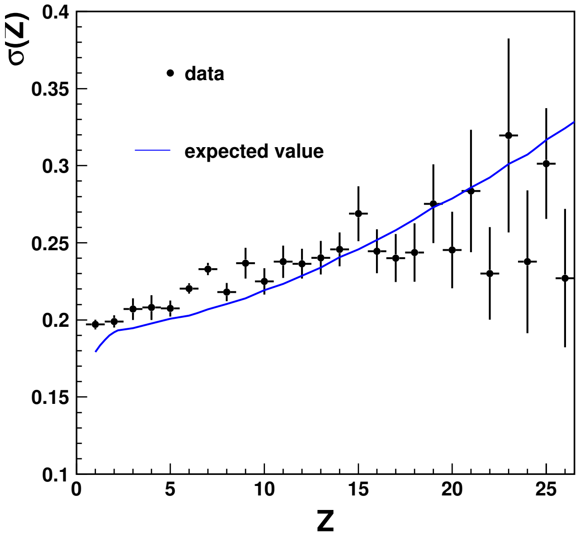

Figure 5.11: Charge resolution versus atomic number. Black markers are data, the continuous line is a theoretical limit (see text).

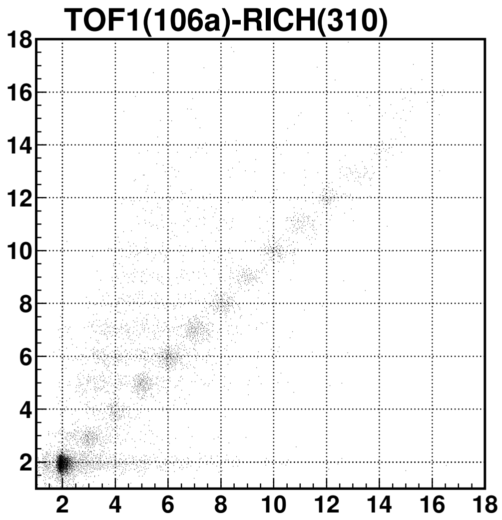

Figure 5.12: Plot of correlation between TOF charge (x axis) and RICH charge (y axis).

(see table 5.4). The charge confusion increases with Z and the results for the data are compatible with the expected value. For Beryllium the data is not available for lack of statistics in TOF data.

atomic number Z	expected value (%)	MC simulation (%)	data (%)
1	0.63	1.27 ± 0.21	0.98 ± 0.10
2	1.18	1.71 ± 0.20	1.55 ± 0.12
3	1.18		1.69 ± 0.76
4	1.20		-
5	1.30		2.63 ± 0.81
6	1.38		1.85 ± 0.66
7	1.57		3.00 ± 0.94

Table 5.4: Charge confusion (%) for data, MC simulatio and the expected value.

5.4 Conclusions

The data taken with cosmic rays are characterised by a wide variety of configurations: events fully contained, or with only a fraction of the ring contained, events with different incidence angle and different velocity.

On the other hand, in the test beam the incident particles are given with a fixed rigidity and fixed direction and most of the events are fully contained.

The configuration with cosmics is surely more "realistic", that is more similar to what we expect with real data on the ISS, but with these data the analysis of the charge is necessarly limited to events with $Z = 1$. Test beam data do offer a wide charge range, but most of them are "golden" events (fully contained) and the results cannot be directly extrapolated to the flight setup.

We conclude that these data somehow complement each other, and from their analysis we can state that:

- the data can be reproduced with a Monte Carlo simulation;
- the dynamic range of the RICH allows charge reconstruction at least up to $Z = 28$;

- the charge resolution deteriorates with increasing Z, as expected, ranging from 0.2, for protons, to 0.3, for Iron;
- the charge confusion decreases with N_{exp} and is $\leq 3\%$ up to $Z = 7$.

Conclusions

The objective of this work is to study the AMS-RICH charge reconstruction capabilities. In order to do it in a complete way, a general overview on CR has been given and the AMS experiment has been described with special emphasis on its RICH detector.

Then, the feasibility of a precise electric charge determination with this RICH detector has been studied. A charge reconstruction algorithm has been developed and tested using both RICH simulation and real data.

From the results obtained on different simulated samples we conclude that the charge resolution ranges from $0.22e$ for protons and increases to $0.28e$ for Aluminum and that for a given species the charge confusion only depends on the number of expected photoelectrons for a kinematically equivalent particle (N_{exp}).

Finally, the reconstruction has been applied to the data taken with the RICH prototype both with cosmic muons and with a beam of ions at CERN SPS. The preliminary analysis of the data shows that the RICH prototype is able to measure the charge spectrum up to at least $Z = 28$ with a charge resolution ranging from $0.2e$ (for protons) to $0.3e$ (for Iron). The charge confusion decreases with N_{exp}, as expected from the simulation, and is $\leq 3\%$ up to $Z = 7$.

Bibliography

[1] K. Ackerstaff, et al. (1998) Nucl. Instr. and Methods A **417** 230

[2] AMS collaboration, (1999) Phys. Lett. B **461**, 387–396

[3] AMS collaboration, Phys. Reports **366** (2002) 331–405

[4] E.G. Anassontzis, et al. (1992) Nucl. Instr. and Meth. A **323** 351-362

[5] W.J. Axford, 18th ICRC (1981) **12** 155

[6] Y. Asaoka et al., Phys. Rev. Lett., **88** 051101 (2002)

[7] G. Barbiellini, et al. (1996) Nucl. Instr. and Methods A **371** 169-173

[8] G. Basini et al., ICRC (1999) **3** 77

[9] R. Bellotti, et al. (1999) Phys. Rev. D, **60** 052002

[10] C.L. Bennett et al., astro-ph 030227 5 june 2003, accepted by the ApJ

[11] M. Boezio et al., ApJ, **518** (1999) 457

[12] M. Boezio et al., ApJ **561** 787 (2001)

[13] Carlson, et al., (1994) Nucl. Instr. and Methods A **349** 577

[14] J. Casaus, Nucl. Phys. B (Proc. Suppl.) **114** (2003) 259–273

[15] J.Casaus, 28th ICRC (2003).

[16] A.J. Davis et al., AIP Conference Proc. **528** 421 (2000)

[17] C. Delgado, master thesis, Universidad Autónoma de Madrid, 2001

[18] C. Delgado, PhD thesis, Universidad Autónoma de Madrid, 2003.

[19] J.J. Engelmann et al., A&A **233**, 96–111 (1990)

[20] L. A. Fisk, et al., ApJ, vol. 190, L35, (1974)

[21] F. Giovacchini, master thesis, University of Bologna, 2003.

[22] Hamamatsu Photonics: http://www.hamamatsu.com

[23] M. Hof, et al., (2000) NIM A, **454**, 180–185

[24] J.R. Jokipii & G. Morfill, ApJ **312** 170 (1987)

[25] J. R. Jokipii, ApJ, vol. 466, L47, (1996)

[26] W.R. Leo, (1987) *Techniques for Nuclear and Particle Physics experiments*, Springer-Verlag

[27] M. Longair, (1994) *High Energy Astrophysics*, vol. I and II, Oxford University press.

[28] Matsushita Electrics Works, http://www.mew.co.jp/e-index.html

[29] F. Mayet, XIth Rencontres de Blois proceedings, (1999)

[30] W. Menn et al., ApJ **533**, Issue 1, 281 (2000)

[31] M. Nagano, et al., (2000) Reviews of Modern Physics **72** 689

[32] Novosibirsk Institute of Catalysis: http://www.catalysis.nsk.su/

[33] S. Orito, et al., (2000) Phys. Rev. Lett. **84** 1078–1081

[34] J.R. Primack, Frascati Physics Series Vol. XXIV (2002) 449–474

[35] R.J. Protheroe & A.P. Szabo, Phys. Rev. Lett. **69** 2885 (1992)

[36] J.P.Rachen et al., A&A **273** 377–382 (1993)

[37] R. Rebolo, Nucl. Phys. B (Proc. Suppl.) **114** (2003) 3–11

[38] O. Reimer, et al., (1998) ApJ, **496**, 490–502

[39] RUNJOB collaboration, 26th ICRC 1999, og 1.2.14

[40] P. Salati et al., 26th ICRC (1999), he.5.1.06

[41] L. Scarsi, Frascati Physics Series Vol. XXIV (2002), 279–296

[42] J. Seguinot, (1998) Cours donné à l'Ecole Joliot-Curie, Maubuisson

[43] M. Simon, Frascati Physics Series Vol. XXIV (2002) 119–136 .

[44] S. Straulino at al., NIM A 478 (2002) 114–118

[45] Super-Kamiokande collaboration, Phys. Rev. Lett. **81**, 3319-3323 (1998)

[46] S.P. Swordy et al., Phys. Rev. Lett. D (1990) **42** 3197–3206

[47] Takahashi, (1998) Nucl. Phys. B (Proc. Supl.) **60B** 83–92

[48] A. Torrentó, master thesis, Universidad de La Laguna, 2003.

[49] P. Ullio, Frascati Physics Series Vol. XXIV (2002) 475

[50] W.R. Webber, (1982) ApJ, **255**, 329.

[51] Ypsilantis & Seguinot (1994) Nucl. Instr. and Meth. A**343** 30–51